Microtubule buckling in an elastic matrix with quenched disorder

Cheng-Tai Lee and Eugene M. Terentjev[1]
Cavendish Laboratory, University of Cambridge, J.J. Thomson Avenue, Cambridge, CB3 0HE, U.K.

The intracellular elastic matrix has been recognized as an important factor to stabilize microtubules and increase their critical buckling force P_c in vivo. This phenomenon was qualitatively explained by the Winkler model, which investigated buckling of a filament embedded in a homogeneous elastic medium. However, the assumption of homogeneity of the matrix in Winkler's, and other advanced models, is unrealistic inside cells, where the local environment is highly variable along the filament. Considering this to be a quenched-disorder system, we use a Poisson distribution for confinements, and apply the replica technique combined with the Gaussian variational method to address the buckling of a long filament. The results show two types of filament buckling: one corresponding to the first-order, and the other to a continuous second-order phase transition. The critical point, i.e. the switch from first- to second-order buckling transition, is induced by the increase in disorder strength. We also discover that this random disorder of the elastic environment destabilizes the filament by decreasing P_c from the Winkler result, and the matrix with stronger mean elasticity has a stronger role of disorder (inhomogeneity). For microtubules in vivo, buckling follows the discontinuous first-order transition, with P_c reduced to the fraction between 0.9 and 0.75 of the Winkler prediction for the homogeneous elastic matrix. We also show that disorder can affect the force-displacement relationship at non-zero temperature, while at zero temperature this effect vanishes.

1. INTRODUCTION

Microtubules (MTs) are rigid linear protein filaments with a large persistence length, of around millimeters, while their total length can vary from nanometers to hundreds of microns. In cells, MTs, together with actin and intermediate filaments, form a cytoskeleton (CSK) network that maintains the cell shape and mechanical response. As the tensegrity model suggested, MTs act as components which resist external compression[1,2] in the overall CSK matrix. It is therefore essential to understand the mechanical response of MTs to the applied compressive forces. Previous experiments and simulations showed that MT buckling is an almost in-plane process[3,4]. The basic mechanical response of an initially straight filament under a compression force P (see Fig. 1) is described by the energy functional[5]:

$$H_E = \int_0^{L_0} dS \left[\frac{K}{2} \left(\frac{d^2 Y}{dS^2} \right)^2 - \frac{P}{2} \left(\frac{dY}{dS} \right)^2 \right], \quad (1)$$

where S is the arc length along the filament contour, K is the bending rigidity, which relates the energy penalty of locally bending to the squared of local curvature[6–9], P is the applied force set to be positive for compression. The small-deflection assumption is used in the
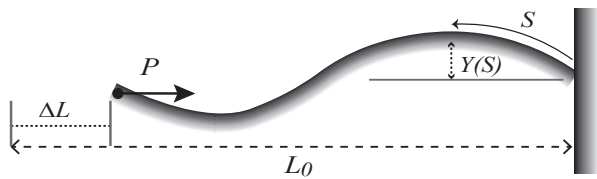

FIG. 1. A sketch of a filament under compression P, illustrating the notations used in the Euler model.

above equation, giving $\frac{1}{2}(dY/dS)^2$ as the local filament displacement along its average axis: the approach commonly adopted for semiflexible chains and vortex lines[10]. The important physical quantities to obtain here are: the force-displacement profile, which is the relation of how much the filament contracts upon increasing compressive forces, and the critical buckling force P_c, which is the threshold to initiate buckling and lose the mechanical stability[5].

Based on the elastic Hamiltonian of Eq. (1), in 1757, Euler derived the relation for the critical buckling force, without thermal fluctuations[5]: the classical expression is $P_c^E = \pi^2 K / L_0^2$ for a filament pinned at both ends, where the numerical factor π^2 may change with different boundary conditions. One may also concider the role of thermal fluctuations that could affect the filament buckling[7,11]. For a semi-flexible filament, thermal fluctuations cause the decrease of the critical buckling force, described as a simple scaling relationship[11]: $P_c/P_c^E \approx 1 - 1.11 (k_B T L_0 / K)^{0.56}$, where K is the bending modulus as in Eq. (1). Thermal effects are less relevant for very stiff filaments, when $k_B T L_0 / K \ll 1$. For a single MT of bending rigidity[12] $K \approx 2 \times 10^{-23}$ N * m² and length $L_0 = 10 \, \mu\text{m}$ at room temperature, this ratio is estimated to be: $k_B T L_0 / K \approx 0.002$. Consequently, thermal fluctuations have only a minor effect on MT buckling.

The Euler buckling model can only describe the single MTs in vitro, while the inclusion of an elastic matrix is more realistic in vivo, where the confinements of the CSK network could act as a source of elasticity. In fact, buckling experiments of single MTs, and the relating theories, have indicated that the embedding elastic matrix is an important factor. A larger critical buckling force P_c and a shorter wavelength of the buckling pattern were observed in vivo[12–14], compared with buckling without a matrix (in vitro). This difference in P_c is qualitatively explained by the classical buckling theories on an

inextensible filament without thermal fluctuations, due to Emil Winkler ca. 1866, which accounts for coupling with an elastic foundation that resists lateral displacement of the filament[5,14]. The Winkler elastic foundation model has the energy, $\frac{1}{2}\gamma Y^2$, added up to the Hamiltonian of Eq. (1), where γ is the elastic modulus of the homogeneous embedding matrix.

For a long filament pinned at both ends, the Euler threshold P_c^E decreases to zero, when the filament length L_0 becomes infinite. In contrast, Winkler obtains a length-independent P_c relation that depends only on bending rigidity K and the elastic modulus of the matrix: $P_c^W = 2\sqrt{K\gamma}$. Therefore, very long filaments are preferentially constrained by the matrix. Our work will focus on the details of the embedding elastic matrix, which both experiments and theory recognized as a crucial factor in MT buckling in vivo.

Although some theoretical papers have developed a more complicated descripton of the elastic matrix than used in the original Winkler model, the same buckling threshold is mostly recovered. An example is a non-linear elasticity model, with both transverse and longitudinal elastic coupling with the matrix[15,16], aimed to explain the decay length of the buckling pattern: it seems that the Winkler expression for P_c^W is very robust. However, we notice an unrealistic pre-assumption in these papers, and in the original Winkler model: the homogeneous elastic matrix. In cells, it implies the confinements of the network have a very small spacing, and the spatial variation of the elastic modulus along the filament is not allowed.

In reality, the intracellular cytoskeleton network[17,18] can be rather disordered and inhomogeneous. This network is also highly dynamic[19,20]. The time-scales for the non-equilibrium soft matrix of cortical cytoskeleton to re-distribute its structure and reach thermal equilibrium are well-studied and are of the order of few minutes. This may be too long to be practically achieved when a microtubule finds itself under an external force, making this a quenched-disorder system. Quenched disorder refers to the 'frozen' heterogeneity that involves random variables which do not evolve with time and thermal fluctuations, due to its slow dynamics. Of course, there may be other in-vitro systems where the embedding matrix is disordered permanently. The effect of such disorder is conventionally formulated as a random potential that exhibits a characteristic probability distribution for each realization of the random variable. It has previously been seen to affect the average properties of polymers or filaments over all possible realizations, in many other different scenarios. For instance, the random potential acting on chain segments shrinks the mean size of the free polymer, inducing the collapse of the chain[21–23]; in filament stretching, the quenched random force exerted from the environment turns out to be an additional source of resistance to the stretching force applied on the filament ends, other than the non-zero temperature effect[24,25]. These studies motivate us to examine the effect of quenched disorder from the CSK confinements (reflected in the local variation of the elastic modulus) on the filament buckling.

The key findings of our paper are: the quenched disorder induces the softening of the matrix before and at buckling (decreasing the effective elastic modulus), and hence causes a decrease in the threshold P_c from the Winkler expression. A critical point, similar to the switch between the first- and the second-order phase transition, appears in this effective elastic modulus and in the associated force-displacement profile, when the disorder strength increases. At buckling with weak disorder, an abrupt jump in the displacement appears, while a continuous change is seen in the strong disorder case. Although we find that thermal fluctuations are less relevant for MT in an inhomogeneous elastic matrix, the theory is capturing their effects, and hence its results remain valid even for longer or less stiff filaments, where thermal effects may become important.

The paper is organized as follows. Section 2.1 is on the the Hamiltonian of the system and the statistical distribution $f[\gamma]$ for the local realizations of the confining modulus $\gamma(S)$. In Section 2.2, we formulate the replica Hamiltonian[26], $H_{\rm rep}[Y(s)]$, required in finding the quench-averaged quantities. This Hamiltonian is not simple, and is Taylor-expanded to the 6th order of Y: the 2nd order of this expansion is the elastic energy with an average elastic modulus, while the effect of strength of disorder is embedded in the negative 4th and positive 6th order terms. In Section 2.3, Gaussian variation method (GVM)[27,28] is introduced to deal with this high-order Hamiltonian. An optimization equation emerges from the requirement of varying the trial Gaussian Hamiltonian, in order to approach the true free energy of the system as closely as possible. In Section 3.1, we exclusively address the optimization equation in the long filament. In Section 3.2, based on this equation, the trial Gaussian is solve as a function of the compressive force and the strength of disorder. Sections 3.2 to 3.5 discuss the consequences of the solved trial function to obtain P_c and $\langle \Delta L \rangle$. To keep the text neat and the logical line clear, many of the detailed derivations are moved to the Appendices.

2. THEORY

2.1. Hamiltonian and quenched disorder distribution

We consider MT as an inextensible filament of length L_0, embedded in an inhomogeneous elastic matrix of the 2D system. The regime before and at buckling is the main interest of this paper, hence imposing the the small-deflection assumption[5,10,15,16,24] to avoid the complexity that could arise in the elastica theory[5]. As a simple model, the matrix is assumed to show linear elasticity only in the lateral direction, with the local elastic modulus $\gamma(S)$, which embodies the nature of randomly-distributed confinements along the filament. The reason
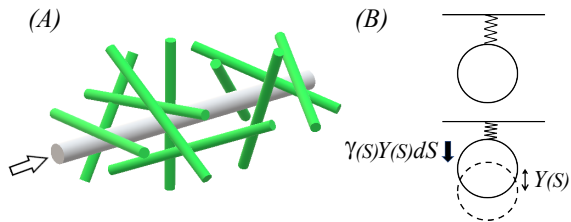
FIG. 2. (A) A filament laterally constrained by randomly-distributed confinements along the axis, imposing local sites of elastic force penalizing the transverse filament displacement. (B) The cross-section viewed from the arrow. An effective spring of elastic constant $\gamma(S)dS$ is used to determine this confining force: $\gamma(S)Y(S)dS$, for the filament segment of length dS.

to exclude longitudinal elasticity is because it showed no qualitative difference in critical buckling force in earlier studies[15,16].

Each realization of the local elastic modulus $\gamma(S)$ throughout the filament contour occurs with the probability given by $f[\gamma(S)]$. Despite inhomogeneity, the elasticity strength of this matrix is measured by its average elastic modulus $\langle\gamma\rangle$. The symbol $\langle\cdots\rangle$ means averaging over all possible realizations of $\gamma(S)$ along the filament contour, through its probability distribution function $f[\gamma]$. Note that our model is reminiscent of Winkler's, yet the local elastic modulus here is no longer a constant. The goal is to use the well-developed replica technique[26,27] to find how strength of quenched disorder enters the critical buckling force $\langle P_c \rangle$ and force-displacement $\langle\Delta L\rangle$.

The Hamiltonian of the system described in Fig. 2 is modified from Eq. (1), by adding an elastic energy stored in the matrix:

$$H = \int_0^{L_0} dS \left[\frac{K}{2}\left(\frac{d^2Y}{dS^2}\right)^2 - \frac{P}{2}\left(\frac{dY}{dS}\right)^2 + \frac{\gamma(S)}{2}Y^2 \right] , \quad (2)$$

where the local elastic modulus $\gamma(S)$ is the quenched disordered variable. To find its statistical distribution $f[\gamma(S)]$, w segments of length Δ_S along the filament are cut from the matrix: $w = L_0/\Delta_S$. Within each Δ_S segment, the elastic modulus for this local segment is assigned the notation γ_i. The same cutting-counting procedure is repeated numerous times for many MT filaments to build up the probability distribution function of the number of confinements N_i^c, for this local segment of length Δ_S. Here, the confinements refer to the filaments that are parts of the intracellular network and have contact with the main filament we are investigating on the surface (see Fig. 2).

This distribution function of N_i^c, however, is not available from previous studies. Yet, it may be tentatively assumed to follow the Poisson distribution, which adopts a constant average rate for occurrence of individual events. In the context here, it means that, on average, it is expected to find one confinement when moving along the
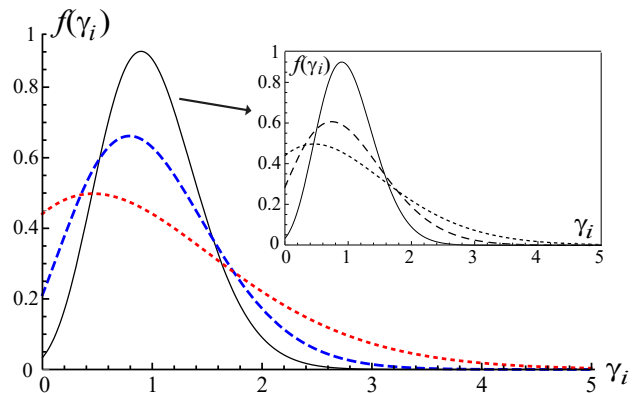

FIG. 3. The distribution function $f(\gamma_i)$, Eq. (3), which depends on the ratio $(\gamma\Delta_S/\varepsilon)$, is plotted at fixed $\langle\gamma\rangle = 1$ and $\Delta_S = 5$. A broadening of the distribution width is observed when the elastic strength of confinement ε is increased: $\varepsilon = 1$ (solid line), $\varepsilon = 2$ (dashed line), and $\varepsilon = 5$ (dotted line). The inset shows $f(\gamma_i)$ at fixed $\varepsilon = 5$ and varying segment length: $\Delta_S = 5$ (solid), $\Delta_S = 3$ (dashed), and $\Delta_S = 1$ (dotted line).

filament contour across a distance ξ, the average spacing between CSK confinements. In fact, the limiting expression of Poisson (when the segment length Δ_S is long enough, it roughly gives a Gaussian with the mean and variance equal to the same value) was already used to formulate the probability distribution of the density of the quenched cross-links[28].

Here, we write the general form of the Poisson distribution with respect to N_i^c as: $(\Delta_S/\xi)^{N_i^c}\exp(-\Delta_S/\xi)/N_i^c!$, where Δ_S shall be multiples of ξ. We can convert this probability of N_i^c into the probability distribution of γ_i, through the relation $\gamma_i\Delta_S = N_i^c\varepsilon$, where ε is the elastic constant a single confinement provides, and the average elastic modulus is given as $\langle\gamma\rangle = \varepsilon/\xi$. Note that ξ and $\langle\gamma\rangle$ are parameters that can be experimentally measured. The direct measurement of ε is not plausible, but its value can be deduced from the relation $\varepsilon = \langle\gamma\rangle\xi$. Therefore, the Poisson distribution we use here can build a connection with the experiments. The elastic constant ε depends on many factors that are not yet specified, such as the orientation or the bending rigidity of the confinements. It is also possible that ε has an entropic excluded-volume contribution proportional to T. However, we do not intend to complicate the problem further, and take the parameter ε as a somewhat averaged value, so as to see more easily the effect of quenched disorder (i.e. the local distribution of the number of confinements along the filament).

The probability distribution $f[\gamma]$ for a $\gamma(S)$ realization throughout the whole filament is simply the product of the probability for each segment:

$$f[\gamma] = \frac{1}{\mathcal{N}}\prod_{i=1}^{w}\frac{\left(\frac{\Delta_S\langle\gamma\rangle}{\varepsilon}\right)^{\gamma_i\Delta_S/\xi}e^{-\Delta_S\langle\gamma\rangle/\varepsilon}}{(\gamma_i\Delta_S/\varepsilon)!} , \quad (3)$$

where $\mathcal{N}$ is the normalization factor, the mean elastic

modulus $\langle\gamma\rangle = \varepsilon/\xi$. Based on this distribution, the variance $(\langle\Delta\gamma_i^2\rangle - \langle\Delta\gamma_i\rangle^2)$ in the segment of length Δ_S is $\varepsilon^2/\Delta_S\xi$ (or equally: $\langle\gamma\rangle\varepsilon/\Delta_S$). For matrices sharing the same average elastic modulus, the choice of ε will affect the disorder strength affecting the local elastic modulus $\gamma(S)$. The matrix with a larger ε, or equally a larger spacing ξ as we hold $\langle\gamma\rangle = \varepsilon/\xi$ at a fixed value, has a broader distribution width of γ_i and thus stronger disorder, if compared in segments of the same length Δ_S. In Fig. 3, we present the width-broadening feature when increasing the disorder measure ε or decreasing the segment length Δ_S, while keeping the same mean elastic modulus $\langle\gamma\rangle$.

When we use the notation $\int D\gamma\, f[\gamma]$ for the path integral over all possible realizations of $\gamma(S)$ along the filament, it means to discretize the filament in segments of length Δ_S first, and then complete the averaging. The quenched disorder free energy F_d of this system is given by: $F_d = -k_B T\langle\ln Z\rangle = k_B T\int D\gamma\, f[\gamma]\ln Z$, where Z is the partition function obtained by integrating over configurations of Y, namely, $Z = \int DY\exp(-\beta H)$ (the expression of H is given in Eq. (2)), and $\beta = 1/k_B T$. Likewise, given a physical quantity 'A' which depends on the specific choice of the $\gamma(S)$ realization, its quenched average $\langle A\rangle$ is estimated by: $\langle A\rangle = \int D\gamma\, f[\gamma]\int DY\left(Ae^{-\beta H}/Z\right)$, with the same definition of Z above. Although simple and clear in concept, the direct implementation of this quenched averaging is algebraically difficult, which, nevertheless, can be overcome by the replica technique[21,26].

2.2. Replica Technique

Replica technique was invented by Edwards and Anderson in 1976[29], to study the spin-glass system, and then widely applied to other quenched disordered systems[21,23,24,30]. The idea is to re-write $\ln Z$ as a limit expression, which facilitates the averaging process by quenched disorder[26,31]: $F_d = -k_B T\langle\ln Z\rangle = -k_B T\left(\partial\langle Z^m\rangle/\partial m\right)|_{m\to 0}$. The first step is to calculate the averaged replica partition function $\langle Z^m\rangle$, with an integer m. This is physically equivalent to averaging the disorder across m replicas of the investigated system with the same Hamiltonian, hence the name. A bald step is then taken: sending the number of replicas m continuously to zero while the averaging $\langle Z^m\rangle$ is done assuming m to be an integer.

Both the disorder free energy and any average $\langle A\rangle$ are usually given through the replica Hamiltonian, $H_{\rm rep}$. Its definition is simply the quenched averaged Hamiltonian of all m replicas, and is the exponent remained after carrying out the $\gamma(S)$ path integral inside $\langle Z^m\rangle$ (without further integration over configurations of the filament deflection), through the relation:

$$e^{-\beta H_{\rm rep}} \equiv \int D\gamma\, f[\gamma]\, e^{-\beta\sum_{a=1}^{m} H[Y_a,\gamma]}, \qquad (4)$$

where $H[Y_a,\gamma]$ is the Hamiltonian of the ath replica: $H_a = \int_0^{L_0} dS\left(KY_a''^2/2 - PY_a'^2/2 + \gamma(S)Y_a^2/2\right)$ from Eq. (2). $Y_a(S)$ is the filament deflection in the ath replica, and the shorthand $'$ and $''$ refer to differentiation with respect to the coordinate S once and twice, respectively. The quenched averaged quantities are expressed through $H_{\rm rep}$ as:

$$\langle A\rangle = \lim_{m\to 0}\int\left(\prod_{a=1}^{m} DY_a\right)A_{\{a,b\}=1}\, e^{-\beta H_{\rm rep}}. \qquad (5)$$

The label '1' used for the replica of the observable 'A' is completely arbitrary, and in fact, the result obtained must not depend on this particular index if the calculation is done correctly.

The calculation of $H_{\rm rep}$ is straightforward[24,26]. The energy terms without $\gamma(S)$ in Eq. (4) are unchanged after completing the path integral over $\gamma(S)$. For terms containing $\gamma(S)$, the standard procedure to carry out this path integral involves a similar discretization process of S and $\gamma(S)$, as described in Section 2.1: cutting each of the total m replicated filaments into w segments of length Δ_S, $w = L_0/\Delta_S$. But this time $Y_a(S)$ is also involved in the path integral, and also needs to be discretized. It is implicitly assumed that the continuous filament deflection functions Y_a in all replicas are smooth and slowly-varying, which is usually true before the buckling occurs. The continuous function $Y_a(S)$ could therefore be reasonably replaced with its discretized version $Y_{a,i}$, the filament deflection of the ith segment in the ath replica.

With the discretized functions $Y_{a,i}$ and γ_i, and the $f[\gamma]$ from Eq. (3), the terms involving $\gamma(S)$ can be integrated in the path integral in Eq. (4), with the use of the Stirling approximation for the factorial and then by finding out the steepest descent of $f(\gamma_i)\cdot\exp\left(-\gamma_i\sum_a Y_{a,i}^2\Delta_S/2\right)$ (see Appendix A). We Taylor-expanded this resultant function in the assumption of small deflections of $Y_{a,i}^2$, which was already adopted in formulating the Hamiltonian in Eq. (2). The expansion has to go to the 6th order term, since we discover that the 4th order term is negative and does not provide system stability. Subsequently we transform the discretized version back to the continuous integral with the approximated $H_{\rm rep}$ written as:

$$H_{\rm rep} = \int_0^{L_0} dS\, \sum_{a=1}^{m}\left(\frac{K}{2}Y_a''^2 - \frac{P}{2}Y_a'^2 + \frac{\langle\gamma\rangle}{2}Y_a^2\right)$$
$$- \sum_{a,b=1}^{m}\frac{\beta\langle\gamma\rangle\varepsilon}{8}Y_a^2Y_b^2 + \sum_{a,b,c=1}^{m}\frac{\beta^2\langle\gamma\rangle\varepsilon^2}{48}Y_a^2Y_b^2Y_c^2, \quad (6)$$

where K is the bending rigidity, P the compressive force, ε the elastic constant of a single confinement, and Y_a the filament deflection along the filament contour S of the ath replica.

The disorder strength in the local confinements of our filament are measured by the distribution width: $\langle\Delta\gamma_i^2\rangle - \langle\Delta\gamma_i\rangle^2 = \langle\gamma\rangle\varepsilon/\Delta_S$. Only the 4th and 6th

5

order terms reflect this disorder effect from confinements through the parameter ε, while the harmonic term $\langle\gamma\rangle Y_a^2/2$ represents the Winkler limit of homogeneous elastic foundation. This can be understood from the fact that to hold a constant mean elastic modulus, a weaker elastic strength ε from a single confinement requires a shorter spacing of confinements (higher confinement density), eventually giving the limiting homogeneous case. On the other hand, when there is no confinement, the mean elastic modulus $\langle\gamma\rangle$ becomes zero, causing the Winkler and higher-order terms to vanish, and the Euler limit is recovered.

A similar problem was considered earlier[32], and only retained to the 4th-order term of the polymer field, also with a negative coefficient. There, the authors introduced the auxiliary field to decouple the 4th-order term, then expanded the resultant Hamiltonian into many harmonic terms, and recognized the divergent term as the main contribution to the 'propagator'. Nevertheless, the physical quantity they were looking for had later to be normalized by all the contributions in this propagator, and thus were able to deal with the resulting instability (divergence). However, this method would not work in our model, as the investigated physical quantities are totally different. We don't have the same normalization process to counter this divergence, and consequently need the 6th order term here to avoid instability.

To find the quenched averaged quantities, we need to insert this H_{rep} back into Eq. (5). We introduce the Gaussian variation method (GVM) for high-order terms, which was first used in the context of random manifolds by Mezard and Parisi[27] and widely applied in quenched disorder systems[23,28]. In particular, our H_{rep} takes a very similar structure to the problem of a free polymer chain in random potential[23]. Before implementing the GVM, we non-dimensionalize Eq. (6) and re-write it in the new non-dimensional variable $s = S/\zeta$ and deflection $y_a = Y_a/\zeta$, where ζ is an arbitrary length scale, which we expect to be the order of MT segment size. We will need to later verify that none of our results depend on the choice of this length scale. We need this parametrization (instead of choosing the length scale to be the filament length L_0) in order to leave the actual MT length L_0 free to change and also recognize the major contributions in the free energy for a long filament, as some results will depend on it.

$$\tilde{H}_{\text{rep}} = \int_0^{l_0} ds \sum_{a=1}^{m} \left(\frac{k}{2} y_a''^2 - \frac{p}{2} y_a'^2 + \frac{\text{æ}}{2} y_a^2 \right)$$
$$- \sum_{a,b=1}^{m} \frac{\eta}{4} y_a^2 y_b^2 + \sum_{a,b,c=1}^{m} \frac{w}{6} y_a^2 y_b^2 y_c^2 \qquad (7)$$
$$\text{with} \quad \eta = \frac{\text{æ}\Delta}{2} \quad \text{and} \quad w = \frac{\text{æ}\Delta^2}{8},$$

where l_0, $\tilde{H}_{\text{rep}}$, k, p, æ and Δ are non-dimensional forms defined by the relations: $l_0 = L_0/\zeta$, $\tilde{H}_{\text{rep}} = \beta H_{\text{rep}}$, $k = \beta K/\zeta$, $p = \beta P\zeta$, $\text{æ} = \beta\zeta^3\langle\gamma\rangle$ and $\Delta = \beta\zeta^2\varepsilon$. The non-dimensional mesh size l_m is accordingly expressed as: $l_m = \xi/\zeta = \Delta/\text{æ}$. y_a'' and y_a' are the second and first derivatives of the filament deflection of the ath replica, with respect to the non-dimensional contour length s. Note that the coefficients η and w are not independent, and in the final results, they will be transformed back to æ and Δ parameters. Eq. (7) is the key result in this section and is the non-dimensional replica Hamiltonian that will be used in the following calculations.

2.3. GVM and the optimization equation

The standard GVM procedures go as follows. The replica Hamiltonian is first cast into Fourier space, to handle any differential terms of the fields y_a in Eq. (7). We use the boundary conditions of a filament pinned at both ends[14], requiring $dy_a/ds = 0$ and $dy_a^2/ds^2 = 0$. The y_a is accordingly written as a sine Fourier series: $y_a = \sum_{n=1}^{\infty} \bar{y}_{an} \sin(n\pi s/l_0)$, where '$n$' is the index for the discrete Fourier modes, $\bar{y}_{an}$ is the Fourier amplitude of the n-th mode in the ath replica. Inserting this series back in Eq. (7), and integrating over s, we obtain:

$$\tilde{H}_{\text{rep}} = \sum_{a=1}^{m} \sum_{n}^{\infty} \frac{l_0}{4} \left[k\left(\frac{n\pi}{l_0}\right)^4 - p\left(\frac{n\pi}{l_0}\right)^2 + \text{æ} \right] \bar{y}_{an}^2$$
$$- \frac{\eta l_0}{32} \sum_{a,b} \sum_{\{n\}} \Gamma_4 \, \bar{y}_{an_1}\bar{y}_{an_2}\bar{y}_{bn_3}\bar{y}_{bn_4}$$
$$+ \frac{w l_0}{192} \sum_{a,b,c} \sum_{\{n\}} \Gamma_6 \, \bar{y}_{an_1}\bar{y}_{an_2}\bar{y}_{bn_3}\bar{y}_{bn_4}\bar{y}_{cn_5}\bar{y}_{cn_6}, \qquad (8)$$

where $\sum_{\{n\}}$ means summing over all Fourier mode indices, the suffixes a and b are replica indexes (summed to the number of total replicas, m), and Γ_4 and Γ_6 are assemblies of many Kronecker-deltas of different Fourier modes (e.g. one of the terms inside Γ_4 is $\delta(n_1 + n_2 - n_3 - n_4)$), produced due to the integral of multiple sin-functions. The full expressions of Γ_4 and Γ_6 are not given here, due to its long length. Instead, the Γ_4 case (i.e. the 4th order case) will be put in Appendix B, for the illustration of algebraic manipulation.

A trial quadratic Hamiltonian in the $\bar{y}_{an}$ functions is assumed to describe the system, which means all physical properties, such as free energy and the quench-averaged quantities, are defined by this new Hamiltonian $\tilde{H}_0$, instead of the original high-order Hamiltonian $\tilde{H}_0$. Although Eq. (8) contains interactions between different Fourier modes, the trial Hamiltonian is assumed to include only the interactions within the same modes. It seems a primary intention of approximation, yet has been shown to very likely capture the key physical essence underlying the problem[23]. It is also important that this trial function does incorporate the interactions between different replicas, which appeared as high-order contributions in our original $\tilde{H}_{\text{rep}}$ and are, in fact, crucial and frequently discussed on their play in the replica

theory[26,27,30,31]. The replica symmetry assumption[26] is further applied, allowing the simplification that only two variational parameters are needed; its stability in this kind of problems has been verified earlier[23]. A more complicated replica symmetry-breaking case will not be presented in this paper. The structure of the trial Hamiltonian is consequently given as:

$$\tilde{H}_0 = \frac{1}{2} \sum_{a,b}^{m} \sum_n \bar{y}_{an} G_{ab}^{-1}(n) \bar{y}_{bn} \ ;$$

$$G_{ab}^{-1}(n) = l_0 \left\{ \Lambda(n)\delta_{ab} + \sigma(n)I_{ab} \right\} \ , \qquad (9)$$

where $G_{ab}^{-1}(n)$ is the element of an $(m \times m)$-matrix at the n-th Fourier mode, with the suffixes a and b for the replica indexes, and m for the total replica number. As often in this type of analysis, I_{ab} is the $(m \times m)$ matrix of ones. Since we see a l_0 factor from all contributions in the replica Hamiltonian of Eq. (7), we expect this l_0 can also be extracted in our trail Hamiltonian. The variational parameters are Λ and σ, and their n-dependence, will be revealed later, when we find out the optimization equation in the GVM, which we are about to address.

The free energy of the original system described by $\tilde{H}_{\rm rep}$ can be cast as an expansion of $\langle \tilde{H}_{\rm rep} - \tilde{H}_0 \rangle_0$:

$$\tilde{F} \approx \tilde{F}_0 + \langle \tilde{H}_{\rm rep} - \tilde{H}_0 \rangle_0 \ , \qquad (10)$$

where $\tilde{F}_0$ is the free energy using the trial Hamiltonian and has the relation: $\tilde{F}_0 = -\sum_n \mathrm{Tr} \ln \underline{G}(n)/2$, and the symbol $\langle \cdots \rangle_0$ means averaging the quantity by the partition of the new trial Hamiltonian $\exp(-\tilde{H}_0)$. The aim of GVM is to minimize Eq. (10) with respect to the variational parameters Λ and σ. The calculation of $\langle \tilde{H}_{\rm rep} - \tilde{H}_0 \rangle_0$ in Eq. (10) is straightforward with the help of the Wick theorem[33], yet lengthy, where the pairing of Fourier modes needs discussion, so as to eliminate the Kronecker deltas in Γ_4 and Γ_6. The full expression of $\tilde{F}$ is derived in Appendix. B, and in the case of a long filament, $\tilde{F}$ is approximately given by:

$$\tilde{F} \approx -\frac{1}{2} \sum_n \mathrm{Tr} \ln \underline{\underline{G}}(n) + \sum_a \sum_{n_1} \frac{l_0 \psi(1)}{2} G_{aa}^{(1)}$$

$$-\frac{\eta l_0}{16} \sum_{a,b} \sum_{\{n\}} \left(G_{aa}^{(1)} G_{bb}^{(2)} + 2\, G_{ab}^{(1)} G_{ab}^{(2)} \right)$$

$$+\frac{w l_0}{48} \sum_{a,b,c} \sum_{\{n\}} \left(G_{aa}^{(1)} G_{bb}^{(2)} G_{cc}^{(3)} + 6\, G_{aa}^{(1)} G_{bc}^{(2)} G_{bc}^{(3)} \right.$$

$$\left. + 8\, G_{ab}^{(1)} G_{ac}^{(2)} G_{bc}^{(3)} \right), \qquad (11)$$

where we move the Fourier mode index of $G_{ab}(n)$ to the superscript by using the shorthand of '1' to '3' for n_1 to n_3, and $\psi(1) = \left(k(n_1\pi/l_0)^4 - p(n_1\pi/l_0)^2 + \ae \right)/2$. The second and third lines of Eq. (11) has the same structure as in Ref.[23], where a similar math procedure was carried out for free polymers (i.e. without the pinning boundary conditions used here, and hence with continuous Fourier

bases). On the other side, for a short-filament, this variational free energy $\tilde{F}$ will have a lot more terms similar in nature to the ones given above. The discarded terms in the full $\tilde{F}$ expression are very likely the contributions from the boundary conditions, and become important in the short-filament case.

In the long-filament case, we can follow the Mézard and Parisi steps[23,27,28], and write $\Lambda(n)$ in the form: $\Lambda = \vartheta(n) + \lambda$, where ϑ is chosen to match the quadratic contributions of Eq. (8). The detailed derivation is given in Appendix C. Overall, we write:

$$G_{ab}^{-1}(n) = l_0 \left\{ [\vartheta(n) + \lambda]\,\delta_{ab} + \sigma I_{ab} \right\} \qquad (12)$$

$$\text{with} \quad \vartheta(n) = \frac{1}{2} \left[k\left(\frac{n\pi}{l_0}\right)^4 - p\left(\frac{n\pi}{l_0}\right)^2 + \ae \right],$$

where the parameters λ and σ are used to account for the quenched disorder effects from the 4th- and 6th-order terms in Eq. (8). In particular, the off-diagonal effect (interactions between two different replicas) is imposed through σ. Noticeably, λ and σ are not n-dependent, and all n-dependence is embedded into $\vartheta(n)$.

The kernel $\vartheta(n)$ of Eq. (12) was also used in the criterion for the critical force in the Winkler model, where the parameters λ and σ accounting for the disorder effect are set to zero in the correlator $G_{ab}^{-1}(n)$. When the compression p is increased and eventually G_{ab}^{-1} is allowed to have a negative value (expecting the divergence in the thermal partition), the buckling occurs. This is equivalent to finding the condition for p that makes the equation $\vartheta(n) = 0$ first have a real solution. When $(n\pi/l_0)$ is treated as a continuous wave vector, we recover the Winkler result: $p_c = 2\sqrt{k\ae}$ in the long filament case.

On the other hand, in the short-filament case, the use of the full expression of $\tilde{F}$ (Appendix. B) will change the n-dependence of Λ in Eq. (9). For example, in the simplified case when only the 4th-order Hamiltonian is used in Eq. (7), $\Lambda(n)$ takes the form $[\psi + \lambda + \sqrt{(\psi + \lambda)^2 - \eta/2l_0}]/2$, where λ is an n-independent variational parameter that shall further be solved, while ψ is the source of the n-dependence defined below Eq. (11). This derivation is given in Appendix C. For the 6th-order case of a short filament, finding n-dependence becomes algebraically implausible, and prevents us from any further analysis of the variational parameters.

We will choose to stay in the long-filament regime, not just due to the complexity the short-filament regime has, but also because earlier experiments have shown that the Winkler model in the long filament regime, rather than in the short-filament case, could provide a reasonable explanation for p_c and buckling wavelength in the intracellular environments[14]. The short-filament case will hence not be addressed in this paper.

The optimization of λ and σ in Eq. (12) is fulfilled by finding the minimum of F in Eq. (11), through the functional derivative $\delta F/\delta G_{ab}(n) = 0$. Generally speaking, σ and λ in Eq. (12) are obtained as functions of the total number of replicas m. The optimized trial

Hamiltonian $\tilde{H}_0$, with the solved λ and σ functions inside, are subsequently placed back in Eq. (5) in the non-dimensional form and Fourier space, then taking the limit $m \to 0$. It turns out that this standard procedure are algebraically implausible, particularly in solving the optimization equation and expressing σ and λ in functions of m.

In fact, if the replica number m is sent to zero, at this step of deriving the optimization equation, the consequent equation is greatly facilitated and becomes mathematically manageable. The solutions obtained following this simplification are λ_0 and σ_0, i.e. taking λ and σ to the limit $m \to 0$, which are the only quantities needed in estimating the quench-averaged values $\langle A \rangle$. Therefore, we use the limit $m \to 0$ here for the equation $\delta F / \delta G_{ab}(n) = 0$ and obtain:

$$G_{ab}^{-1}(n) \approx l_0 \; \vartheta(n) \; \delta_{ab}$$
$$+ \frac{l_0}{2} \left(-\eta \sum_{n_1} G_{ab}^{(1)} + w \sum_i^m \sum_{\{n\}} G_{ai}^{(1)} G_{ib}^{(2)} \right) I_{ab}. \quad (13)$$

Note that the term $\sum_i^m \sum_{\{n\}} G_{ai}^{(1)} G_{ib}^{(2)}$ still has m-dependence buried inside. To remove this m-dependence, the structure of G_{ab} is required. The inverse G_{ab}^{-1} in Eq. (12) can easily be transformed to give G_{ab} as:

$$G_{ab}(n) = \frac{1}{l_0(\vartheta + \lambda)} \left[\delta_{ab} - \frac{\sigma}{(\vartheta + \lambda + m\sigma)} I_{ab} \right]. \quad (14)$$

Inserting Eqs. (12) and (14) into Eq. (13) and comparing the off-diagonal and diagonal elements gives two equations of σ and λ, under the limit $m = 0$. The first equation takes the form:

$$\lambda_0 = -\frac{\eta}{2l_0} \left(\sum_n \frac{1}{\vartheta + \lambda_0} \right) + \frac{w}{2l_0^2} \left(\sum_n \frac{1}{\vartheta + \lambda_0} \right)^2 , \quad (15)$$

where the subscript of λ_0 indicates that this is the λ solution in the limit $m = 0$. Since the right hand side of Eq. (15) has summing up of the n-dependence in ϑ, λ_0 does not depend on 'n'. We remind again that when there is no disorder (i.e. $\eta = w = 0$), this equation gives $\lambda = 0$, as expected in the Winkler model.

The second optimization equation would give $\sigma_0 \cdot \varphi = 0$, where φ is a function of p, k, $\ae$, l_0 and λ_0. If σ_0 is arbitrary, the function φ is required to be zero, which accordingly generates another equation for λ_0. It is unlikely that this equation would match Eq. (15). To allow a possible solution for λ_0, p (the only adjustable parameter) will have to be a specific value, which is unlikely to still be physically reasonable (e.g. p may be required to be a complex number). Instead, a more practical and rather trivial solution is adopted: $\sigma_0 = 0$, making the correlator G_{ab}^{-1} of the trial Hamiltonian a diagonal matrix. Note that this diagonal form of the trial Hamiltonian is not uncommon, and has first emerged in the Edwards-Muthukumar work[21].

3. RESULTS AND DISCUSSION

3.1. The limit of long filaments

In Section 2.3, we elected to stay at the long-filament regime and give the expression of $\vartheta(n)$ in Eq. (12). In this regime, the sum $\sum_n$ in Eq. (15) can be replaced with the continuous integral $\int dn$. We set the wavenumber $q = n\pi/l_0$, therein $\int dn \to l_0 \int dq/\pi$, with the lower limit of the q-integral being π/l_0 (the upper limit remains infinite, in what we assume to be a continuous filament). From the term $\vartheta + \lambda_0$ in Eq. (12), the disorder effect is incorporated with the averaged elastic modulus $\ae$, giving the effective elastic modulus α: $\alpha = \ae + 2\lambda_0$. We will also replace λ_0 with this effective elastic modulus α. Equation (15) is re-written in q and α as:

$$\alpha = \ae - \eta B + w B^2 ; \quad (16)$$
$$\text{with} \quad B = \frac{2}{\pi} \int_{\pi/l_0}^{\infty} \frac{dq}{kq^4 - pq^2 + \alpha} ,$$

where α is the effective elastic modulus defined as: $\ae + 2\lambda_0$. The B-integral above exhibits two different types of divergence behavior when plotted against p, depending on the value of the lower integral limit π/l_0 (in other words, for long and short filaments). This can be observed from the denominator inside the integral: $\left(kq^4 - pq^2 + \alpha \right)$. The divergence occurs when the q value in the integrating range makes this denominator zero.

We gradually increase p from zero, and define p^* as the value that can first have this denominator diminish to zero at a specific wavenumber q^*. These two values p^* and q^* are easily found out from the quadratic $kq^4 - pq^2 + \alpha = 0$, and given as:

$$p^* = 2\sqrt{k\alpha} \; ; \; q^* = \sqrt[4]{\alpha/k}. \quad (17)$$

If the lower integral limit π/l_0 is smaller than q^* at $p = p^*$, the B-integral diverges. This p^* expression is reminiscent of the critical buckling force p_c for a long filament in the Winkler model, but here we have the effective elastic modulus α that contains the disorder effect, instead of the average elastic modulus $\ae$ without this effect. On the other hand, if $(\pi/l_0) > q^*$ at $p = p^*$ (in the short-filament regime), the B-integral will not diverge, until the q solution of the equation, $kq^4 - pq^2 + \alpha = 0$, eventually overlaps with the lower limit π/l_0, when one further increases p beyond p^*. This will give the divergence that depends on the filament length l_0. We will not further discuss this interesting result, and only focus on the long-filament regime, which the expression of our correlator G_{ab}^{-1} is based in.

Here we obtained a more concrete condition to identify the long-filament regime: $l_0 > \pi(k/\alpha)^{1/4}$, and also realize that the B-integral diverges at $p = 2\sqrt{k\alpha}$. For a really long filament ($l_0 \to \infty$), the B-integral will take

the limiting form:

$$B = \frac{1}{\sqrt{\alpha}\left(2\sqrt{k\alpha} - p\right)^{1/2}} \, , \qquad (18)$$

which only covers the regime $2\sqrt{k\alpha} - p > 0$ before divergence occurs, while the regime $2\sqrt{k\alpha} - p < 0$ has no real physical meaning.

To include the effect of the finite filament length in this regime, one has to add extra terms in series expansion of $1/l_0$, but such a correction is not necessary for the case of MT inside the cell. We choose the length scale ζ to be 10 nm (roughly the size of the tubulin dimers[34], which are the basic units composing MT filaments), then insert reasonable values of the parameters k (with the bending rigidity[12,35,36] K between 10^{-23} and 10^{-24} N m^2) and the α values between 10^{-1} and 10 (covering the experimentally-determined elastic modulus of the cell matrix, of a few kPa[17,37,38]), and compare the numerical results with Eq. (18). The long filament turns out to be a good approximation for an MT of length above 3 μm (the range of the MT length commonly seen in in-vivo experiments[14]). We hence use Eq. (18) for the remaining calculations: to solve Eq. (16) with Eq. (18) for $B(\alpha, p)$, insert λ_0 and σ_0 back into $\tilde{H}_0$ of Eq. (9), and replace $\tilde{H}_{\rm rep}$ with $\tilde{H}_0$ in calculating Eq. (5).

3.2. Solution path of the effective elastic modulus α

In order to investigate how the increase of the compressive force p affects the quenched averaged quantities of the system, the optimization Eq. (16) should solved for α as a function of p. However, this will not produce an exact analytical expression. Instead, it is more practical to obtain p as an analytical function of α instead, and find out the resultant implications parametrically. From the quadratic Eq. (16), p is solved as two functions:

$$p_\pm = 2\sqrt{k\alpha} + \frac{w(\text{æ} - \alpha) - \frac{\eta^2}{2}\left(1 \pm \sqrt{\frac{4w(\alpha - \text{æ})}{\eta^2} + 1}\right)}{\alpha\left(\text{æ} - \alpha\right)^2}. \quad (19)$$

To estimate the non-dimensional parameters, we take a rather soft cell matrix that gives the mean elastic modulus $\langle\gamma\rangle \approx 1$ kPa (this value can vary from 1 kPa to 10 kPa in experiments[17,37,38]), and use the bending stiffness of a MT from Gittes et al. [12]: $K \approx 2 \times 10^{-23}$ N m^2 as an example. The elastic strength of a single confinement is calculated from the relation $\langle\gamma\rangle = \varepsilon/\xi$, where the mesh size ξ of the intracellular matrix was found to be between 30 and 60 nm[39,40]. Yet, we deliberately let the mesh size ξ be a varying parameter, not restricted to the experimentally-observed range. We then have an adjustable ε and therefore an adjustable disorder strength $\eta = \text{æ}\varepsilon/2$, to examine the limiting case of the Winkler model. Under the room temperature 300 K and
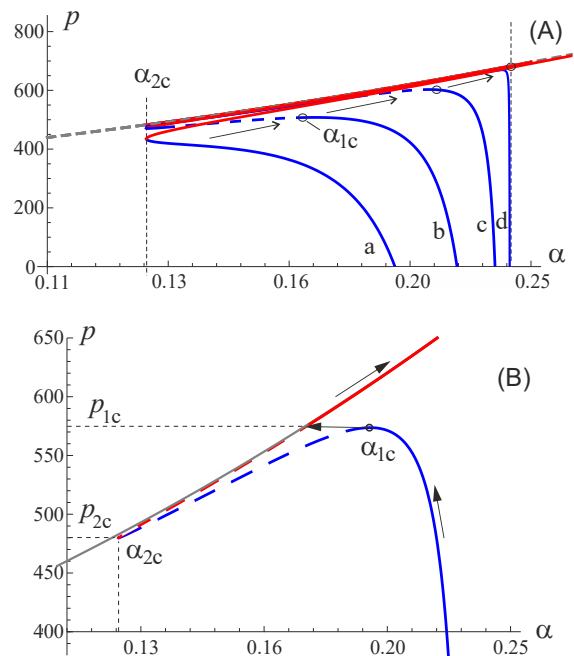

FIG. 4. (A) $p_\pm(\alpha)$ at varied disorder strength η with $k = 4.8\times10^5$ and $\text{æ} = 0.24$: p_+ and p_- are plotted in blue and red, respectively. The thick grey dashed line is the asymptote for p_-, $p = 2\sqrt{k\alpha}$. Its intersection with the vertical asymptote of p_+, i.e. $\alpha = \text{æ}$, gives the Winkler result $p = 2\sqrt{k\text{æ}}$. The curves from (a) to (d) are plotted with $\eta = 5.8, 2.9, 1.5$ and 0.03 (corresponding to the mesh size ξ=200, 100, 50 and 1 nm). The peak of p_+ is shown as a circle, which disappears at strong disorder, see curve (a), but when present, it gradually reduces to the Winkler result as the disorder strength declines, indicated by the arrow. α_{1c} are α_{2c} are buckling points at first- and second-order transitions. (B) The zoom-in picture at the peak of the curve (c) to show the discrete jump of α at the first-order buckling transition. The arrow indicates how the $\alpha(p)$ solution moves with increased compression. p_{1c} and p_{2c} are critical buckling forces of the first and second-order transitions, respectively.

the length scale $\zeta = 10$ nm (chosen to roughly be the size of the tubulin dimers along the MT axis[34]), these parameters give the non-dimensional expressions $k \approx 4.8 \times 10^5$ and $\text{æ} \approx 0.24$, see Eq. (7). Note that w is not independent of η: $w = \eta^2/2\text{æ}$. With these non-dimensional parameters, we plot the solution $p(\alpha)$ in Fig. 4.

The p_+ function originally has two branches, one of which stays in the regime $2\sqrt{k\alpha} - p < 0$, making B-integral in Eq. (18) physically meaningless, and therefore has been discarded (not shown in Fig. 4). The p_- function has the asymptote of $p = 2\sqrt{k\alpha}$ (by observing no divergence at $\text{æ} = \alpha$ and then taking the limit $\alpha \to \infty$), and governs the high-p regime. If the α solution along this p_- function is put back into the correlator G_{ab}^{-1} of Eq. (12) (with λ there replaced with $(\alpha - \text{æ})/2$ and letting $\sigma = \sigma_0 = 0$), it almost gives a zero value, indicating that filament deflection can be very large. Thus, p_- is recognized to be the post-buckling regime.

To investigate the behavior before/at buckling, the p_+ function in Eq. (19) is the focus. At $p = 0$, the effective elastic modulus α is smaller than the average modulus æ, as p_+ function always sits to the left of its vertical asymptote $\alpha = $ æ. An increase in p along the p_+ function gradually decreases α. Since p_- has been recognized as the post-buckling regime, the initiation of filament buckling is thought of as the switch of α solution from p_+ to p_- that would exhibit different mechanical behavior.

To find out this critical compression for buckling, we observe how p_+ evolves to give the Winkler result in Fig. 4A. We remind that the Winkler model is the case where the disorder strength η goes to zero. It requires the mesh size l_m and the elastic strength of one confinement Δ to be extremely small, while holding their ratio a constant, so that mean elastic modulus æ will not vanish in the relation æ $= \Delta/l_m$ (cf. Eq. (7) for definitions of non-dimensional parameters). The Winkler result gives the critical buckling force $p_c = 2\sqrt{k\text{æ}}$, see the discussion of ϑ below Eq. (12).

We notice that the peak of p_+ is the only unique point that moves towards the Winkler result as disorder strength decreases. Consequently, it is recognized as the critical buckling point, giving a sudden jump from the p_+ branch to the post-buckling regime p_-. The overall α solution path is shown as a solid line in Fig. 4B: α gradually decreases as p increases and has a sudden jump at the buckling transition α_{1c}. This discrete jump of α is analogous to the first-order phase transition, and was also seen in the buckling of semi-flexible filaments under thermal fluctuations[11], although the model there did not include the effect of the embedding matrix.

We also notice that the peak of p_+ disappears at stronger disorder, see the curve (a) in Fig. 4. In this scenario, there is only one single-valued α solution as p increases. The α solution path will no longer show a discontinuous jump. The switch from p_+ to p_- becomes continuous, while maintaining the feature of a gradual decreased α upon increased compression, before this switch occurs. An analogy between the disappearance of the α jump and the critical point in the phase transitions could be drawn. Here, the sudden jump in α (at weak disorder) resembles the first-order phase transition. At strong disorder, although α is continuous, the derivative $d\alpha/dp$ is discontinuous at the transition point of p_+ to p_-, hence the filament buckling in this regime is recognized as the second-order phase transition.

3.3. Critical value of the effective elastic modulus

In the weak disorder case, the approximation for the critical value, α_{1c}, can be obtained by Taylor-expanding p_+ of Eq. (19) around $\alpha = $ æ to the third order, which then is used to solve the equation $dp_+/d\alpha = 0$ and find out the peak position of p_+. For strong disorder, the switch happens at the connection point of these two p functions of Eq. (19), described by the equation $p_+ = p_-$

that is analytically solvable to give the exact expression of α_{2c}. The expressions for α_{1c} and α_{2c} take the form:

$$\frac{\alpha_{1c}}{\text{æ}} \approx 1 - \left(\frac{2\eta^2}{\text{æ}^{7/2}k^{1/2}}\right)^{1/3} = 1 - \left(\frac{\Delta^2}{2\text{æ}^{3/2}k^{1/2}}\right)^{1/3} \; ;$$

$$\frac{\alpha_{2c}}{\text{æ}} = \frac{1}{2} \; , \tag{20}$$

where the subscript 1 and 2 refer to the points of first- and second-order transition, respectively. These two critical expressions of α can be inserted back into Eq. (19), to find out the critical buckling force (explored in the next section).

When transforming Eq. (20) back into the dimensional form, the factor of the inverse thermal energy β cancels off on both sides. The decrease of α_c is purely due to the quenched disorder (from the disorder strength η), rather than the thermal effect. This result is intuitive and reasonable, as the structure of the matrix is quenched and will not re-distribute itself by thermal fluctuations, therefore exhibiting no thermal effects in the effective elasticity of the matrix. Since α_c does not depend on temperature, it also follows that the trigger of the critical phenomenon (the cross-over from α_{1c} to α_{2c}) is not due to the thermal effects and is induced purely by the quenched disorder.

We plot Eq. (20) in Fig. 5, with three æ values that sit within the experimental range from 1 to 10 kPa. For clear comparison, we choose the mesh size $l_m = \Delta/\text{æ}$ as the variable, and the result is also expressed in scaled $\alpha_c/\text{æ}$. A larger mesh size with a constant æ indicates a higher disorder strength (from the relation $\eta = \text{æ}^2 l_m/2$). At $l_m = 0$ (no disorder), Eq. (20) is simply reduced to the Winkler model, $\alpha_{1c} = $ æ. An increase in the disorder strength gradually decreases the α_{1c} value, as the disorder has already been known to cause the softening of the elastic matrix in the α solution path in Section 3.2. It is also noticeable that the matrix with a higher mean elastic modulus æ is more sensitive to the disorder effect of expanding the mesh size, due to the factor of æ^2 in disorder strength. Physically speaking, at a fixed mean mesh size, a higher mean elastic modulus indicates a stronger elastic support from the confinement. Any change of the spacing between two confinements due to the random distribution can have a more dramatic effect in the local elastic modulus, hence stronger disorder.

We note that the decrease in α_c from increasing disorder strength is not limitless. Beyond the threshold Δ_c, α_c switches form α_{1c} to α_{2c} and stays as a constant, no matter how disordered the matrix further becomes, see the dashed horizontal line in Fig. 5. The threshold Δ_c for the cross-over from α_{1c} to α_{2c} can be roughly estimated by equating $\alpha_{1c} = \alpha_{2c}$, which gives:

$$\Delta_c \approx \frac{1}{2}\sqrt[4]{k\text{æ}^3} = \text{æ} \cdot \frac{1}{2}\sqrt[4]{\frac{k}{\text{æ}}} \; , \tag{21}$$

where the expression, $0.5(k/\text{æ})^{1/4}$, has the physical meaning of the mesh size, and is similar in structure to the buckling wavelength given in the Winkler model,
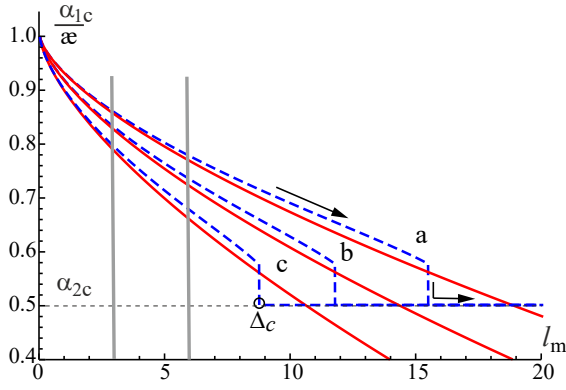
FIG. 5. The normalized α_c plotted against the non-dimensional mesh size l_m, with $k = 4.83 \cdot 10^5$ and $\text{æ} = 0.24$ (set a, 1 kPa), 0.72 (b, 3 kPa) and 2.4 (c, 10 kPa). In particular, the range of the mesh size observed in the intracellular matrix is indicated by two grey lines, from $l_m = 3$ to 6. Each set (a,b,c) contains three curves. The dashed curve is the numerical solution of α_c, with the critical point is indicated by Δ_c. The solid line is based on the approximated α_{1c} given in Eq. (20), while α_{2c} is shown in the dashed horizontal line, and is universal for these three sets, since α_{2c} is normalized by æ. As an example, the arrows in the set (a) are used to show the flow of α_c with increasing mesh size.

$2\pi(k/\alpha)^{1/4}$, yet shorter. The approximation for Δ_c is rather crude, but it has the benefit to give 'the upper boundary' for Δ_c, as shown in Fig. 5. Qualitatively speaking, the approximate Eq. (21) shows that a less rigid filament or a stronger elastic matrix is easier to induce the critical phenomenon by increasing the mesh size from the homogeneous limiting case ($l_m = 0$).

As one may be concerned that the critical phenomenon may originate from the failure of our continuum model for the discretized Hamiltonian, this expression enables the self-check of our assumption of slow-varying deflections at the critical phenomenon, by comparing the most dominant buckling wavelength with the mesh size. The details are moved to Appendix D, and we find that the critical phenomenon we discover satisfies this requirement and our continuum model used for the discretized Hamiltonian still holds validity.

3.4. Critical buckling force

The critical buckling force in the weak and strong disorder regimes (associated with the discontinuous, and the continuous buckling transition, respectively) can be calculated by inserting α_c of Eq. (20) into $p_+(\alpha)$ of Eq. (19):

$$\frac{p_{1c}}{2\sqrt{k\text{æ}}} \approx 1 - \left(\frac{\eta^2}{32k^{1/2}\text{æ}^{7/2}}\right)^{1/3} = 1 - \frac{\Delta^{2/3}}{2^{7/3}k^{1/6}\text{æ}^{1/2}} \; ;$$

$$\frac{p_{2c}}{2\sqrt{k\text{æ}}} = \frac{1}{\sqrt{2}} - \frac{\eta^2}{k^{1/2}\text{æ}^{7/2}} = \frac{1}{\sqrt{2}} - \frac{\Delta^2}{4k^{1/2}\text{æ}^{3/2}} \; , \quad (22)$$
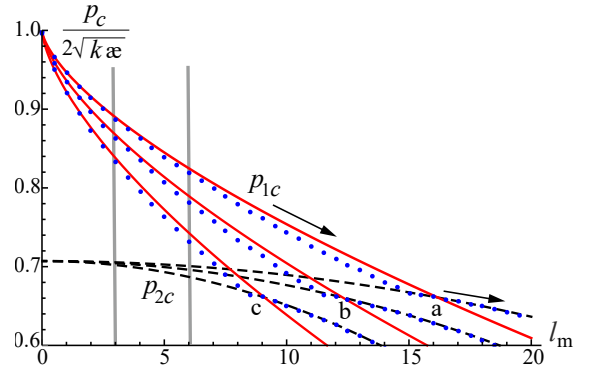

FIG. 6. Normalized plot of p_c against the mesh size l_m, with $k = 4.83 \cdot 10^5$ and $\text{æ} = 0.24$ (set a, 1 kPa), 0.72 (b, 3 kPa) and 2.4 (c, 10 kPa). The range of the mesh size in the intracellular matrix is the regime between two grey vertical lines. Each set (a,b,c) has three curves. The numerical solutions are presented as dotted lines. The approximated expression p_{1c} given in Eq. (22) is solid lines, while p_{2c} curves are presented as dashed lines. The critical point occurs roughly around the intersection of the p_{1c} and p_{2c} lines. The arrows in the set (a) are used to show this cross-over of p_c, as an example.

where p_{1c} is the approximated expression obtained from the Taylor expansion in terms of the disorder strength η. Figure 4 illustrates the positions of p_{1c} and p_{2c} in the α solution path. These two p_c relations cross over from one to the other at a point Δ_c in Eq. (21), when plotted against the mesh size l_m for each specified elastic modulus æ, as shown in Fig. 6, using the same parameters and variables as Fig. 5. A somewhat better estimation of the crossover threshold, which corresponds to the critical point in the phase-transition language, can be obtained by solving the equation $p_{1c} = p_{2c}$. However, it gives a cubic equation for Δ_c, and it is not worth examining, given all our approximation.

Both p_{1c} and p_{2c} decrease when the disorder strength η increases (i.e. the mesh size l_m expands, or the confinement strength $\Delta = l_m\text{æ}$ reinforces). For p_{1c}, this disorder effect adds a correction term to the Winkler result $2\sqrt{k\text{æ}}$. This is due to the softening of the matrix (the effective modulus α is declining with increased compression), with α_{1c} put back in Eq. (19). The first term there is a reminder of the Winkler result, but the average elastic modulus æ is replaced with the 'effective' modulus α, while the second term is a complicated combination of α and also the disorder strength η itself (recall that $w = \eta^2/2\Delta$). Both of these contributions are important in the first-order buckling. When divided by the Winkler result, the ratio of the disorder term has the scaling of $\Delta^{2/3}$, with the bending rigidity k in the denominator, working to counter the effect of disorder. Similar to the discussion on the disorder effect in Fig. 5 of α_{1c}, a higher elastic modulus with a constant mesh size gives a stronger disorder, measured by the factor $\text{æ}^2 l_m$. Hence, decrease in the critical buckling force p_{1c} is more pronounced for a matrix with stronger elasticity, as we see Fig. 6.

As for the continuous buckling transition at p_{2c}, although α_{2c} is a constant value of æ/2 after the critical point, the second term of Eq. (19) can still account for the disorder effect when increasing the disorder strength, while the first term remains unchanged. Overall, a similar result is recovered, with a different numerical factor in front of the Winkler expression and a larger scaling exponent of Δ in the disorder term: Δ^2. The bending rigidity and the mean elastic modulus also play the same role as in the p_{1c} case, yet with larger scaling exponents. It indicates that the change in the buckling force in the second-order transition regime is more sensitive to both intrinsic (k) and extrinsic (æ and Δ) mechanical parameters.

At very large disorder strength, measured by the magnitude of $\eta = \text{æ}\Delta/2$, the expression for p_{2c} loses validity, so the possible zero or even negative critical buckling force are certainly not physical. The replica-symmetrical solution that we are using here does not remain stable at very high disorder strength[28,41]. We are not interested in this regime because it is well outside the range of reasonable parameters in cytoskeleton network: the mesh size is between 30 to 60 nm[39,40] and the elastic modulus is of a few kPa[17,37,38]. The three red curves confined by grey lines in Figs. 5 and 6 cover this in-vivo range, all falling in the first-order transition regime and away from strong disorder limit.

Consequently, buckling of MTs in vivo resembles the first-order transition, with p_c decreased to the fraction between 0.9 and 0.75 of the Winkler prediction. The critical buckling wavelength is estimated by the relation $\lambda_c = 2\pi(2k/p_c)^{1/2}$, derived in Appendix D, Eq. (D2). Since p_c in our model is lower than the Winkler result, the buckling wavelength λ_c is accordingly longer.

Equation (22) can be transformed back into the dimensional form, giving:

$$\frac{P_{1c}}{2\sqrt{K\langle\gamma\rangle}} \approx 1 - \frac{\varepsilon^{2/3}}{2^{7/3}K^{1/6}\langle\gamma\rangle^{1/2}} \; ;$$
$$\frac{P_{2c}}{2\sqrt{K\langle\gamma\rangle}} = \frac{1}{\sqrt{2}} - \frac{\varepsilon^2}{4K^{1/2}\langle\gamma\rangle^{3/2}} \; . \qquad (23)$$

The expressions for the critical buckling force P_{1c} and P_{2c} do not depend on temperature. It is known that thermal fluctuations can affect the P_c expression in the semi-flexible filament[11]. In our free energy formulation, we did include the thermal factor β in the exponent of the partition function in Eq. (5), so one may expect our P_c expression should also manifest the thermal effect. However, we have to take a closer look at the origin of the thermal effcts on P_c in Ref.[11]. The free energy they derived actually had a different physical meaning from ours. They were able to specifically calculate the free energy under the displacement constraint ($\Delta L = $ constant), so that they could recognize at which displacement value the most probable state occurs, and whether more than one stable state exist (and what is the barrier between them).
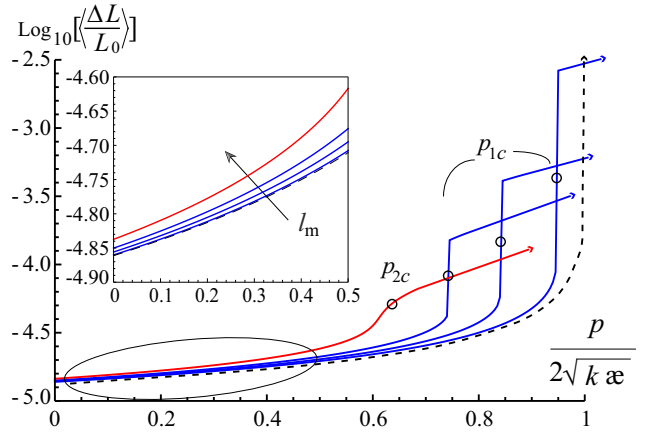

FIG. 7. Log-plot of the normalized displacement $\langle\Delta L\rangle$ against compression p, with $k = 4.8\cdot10^5$ and æ $= 0.24$, at $l_m = 1, 5, 10$ (blue from right to left) and 20 (red). The Winkler result is shown in dashed line. The circle at each curve is the critical buckling point, which gradually evolves from right to left, and eventually switches from the p_{1c} regime to p_{2c}, as the mesh size l_m (the measure of disorder strength) increases. The inset is the zoom-in at small compression, where the quenched disorder already affects the displacement at zero compression.

On the other hand, the free energy we obtain here does not have this displacement constraint, and is the Gibbs free energy at constant applied compression calculated by including all the possible states of varied ΔL values. This consequently blurs the information on the free energy barrier between two or multiple possible stable states, in terms of varied ΔL values. As a result, it prevents us from further exploring how compressive force will reduce this barrier to be comparable with thermal energy and hence induce buckling. This is the limitation of our (Gibbs) formalism.

We will not state that temperature does not have any effect on P_c in buckling inside a quenched elastic matrix. But such thermal effect is expected to be small, when the thermal energy can hardly bend single elastic confinements. In this context, our P_c expressions in Eq. (23) show that the quenched disorder of the confinements inside an elastic matrix is a key athermal factor that affects the critical buckling force.

3.5. Force-displacement profile

The filament contraction ΔL under the small-deflection assumption we used in Eq. (2) is: $\Delta L = \frac{1}{2}\int dS \; (dY/dS)^2$, which can easily be non-dimensionalized (following the same procedure in the end of Sec. 2.2), recast in the Fourier space, and re-written as a continuous integral over the wavenumber q: $\Delta L/L_0 = l_0 \int dq \; q^2\bar{y}_q^2/2\pi$. The quenched averaged displacement $\langle\Delta L\rangle$ by the definition from Eq. (5) is obtained using the average $\langle\bar{y}_q^2\rangle$, calculated in Eq. (D1).

Appendix E gives the detail of $\langle\Delta L\rangle$ calculation:

$$\left\langle\frac{\Delta L}{L_0}\right\rangle = \frac{1}{4\sqrt{k}}\frac{1}{\left(2\sqrt{k\alpha}-p\right)^{1/2}} \qquad (24)$$

$$\approx \frac{k_B T}{4\sqrt{K}}\left(\frac{1}{\sqrt{2\sqrt{K\langle\gamma\rangle}-P}} + \frac{\varepsilon\sqrt{K}}{4(2\sqrt{K\langle\gamma\rangle}-P)^2}\right),$$

where $\alpha(p)$ is the function discussed in Section 3.2, Eq. (19). The second line in Eq. (24) is the approximation at weak disorder and low compression.

Figure 7 shows the force-displacement profile with a fixed value of the mean elastic modulus æ and bending rigidity k in each curve, while varying the disorder strength (measured by l_m). It has several features: the disorder strength shifts the critical buckling force from the Winkler result to a smaller value, and the discrete jump in the displacement (induced by the discontinuity in the α solution path, blue curve) will eventually disappear and become continuous (red curve). This is the conclusions we discussed in Sections 3.2 and 3.4. On the other hand, the inset in Fig. 7 shows the approximate range of filament bending before the buckling threshold, where the second line of Eq. (24) can be applied. This approximation of the displacement gives two types of filament undulation that exist even at zero compression, and importantly, both of them have a thermal factor $k_B T$.

The first type of the undulation is purely due to thermal fluctuations, and this effect has also been seen in other filament stretching or compressing phenomenon investigated with the similar free energy calculation method[11,25]. Yet, the earlier work only examined a filament without an elastic foundation, and gave this thermal term as proportional to $k_B T L_0/K$ (at zero compression and in the small-deflection regime)[11,25]. A long filament is easily bent by thermal fluctuations. In contrast, our thermal undulation term in Eq. (24) gives the ratio $k_B T/K^{3/4}\langle\gamma\rangle^{1/4}$ at zero compression. The thermal energy is balanced by a combination of the elastic support and the bending rigidity, while the effect of the filament length L_0 is lost. For a long filament, the elastic constraint of the matrix is a more important factor in resisting the external compression. This observation is the conclusion Winkler reached in 1866, when investigating the critical buckling force at zero temperature.

The second type of filament undulation is a combination of both thermal and quenched disorder effects. In many other quenched disorder problems (e.g. in random local filament-curvatures[42] or random environmental force[25]), the disorder is entered as an independent term without coupling with thermal energy, and still exists at zero temperature. But in our model, the disorder in the CSK matrix vanishes at zero temperature.

This difference in disorder effect on filament bending can be understood by looking at our trial Hamiltonian $\tilde{H}_0 = l_0 \int dq(kq^4 - pq^2 + \alpha)\bar{y}_q^2/2$, and realizing that the fully-stretched straight filament is the most stable state at $T=0$ in our model before the buckling occurs. In this scenario, the disorder embedded inside the effective elastic modulus α will therefore not be present. In contrast, in the cases of disordered local filament curvatures, or the random environmental force, the most stable state at $T=0$ is not the fully-stretching state, and depends on the detailed configurations of the disorder variables. It consequently gives the quenched-disorder dependence of the displacement, regardless of the presence of thermal effects.

4. CONCLUSIONS

We examine the buckling of a long filament embedded inside an inhomogeneous elastic matrix, where the quenched disorder originates from the distribution of confinements along the filament. We find that an analogy with first- and second-order phase transitions can be drawn in the buckling behavior, with the order parameter being the effective elastic modulus. This order parameter is found to be temperature-independent. The switch from the first-order to second-order transition, i.e. the critical point, is induced purely by the strength of quenched disorder.

In either type of buckling, the quenched disorder in elastic matrix is found to shift the athermal critical buckling force from the Winkler result $P_c = 2\sqrt{K\langle\gamma\rangle}$ to a lower value. Hence, the disorder inside the matrix deteriorates its ability to support and stabilize the filament. This destabilization is also seen in the filament bending at non-zero temperature before buckling. Specifically for MTs in vivo, P_c is reduced to the fraction between 0.9 and 0.75 of the Winkler prediction, with buckling behaviour resembling the first-order phase transition. This effect, of random disorder destabilizing the effective elastic matrix, has been seen before in different context; for example, in the scaling analysis of Cates & Ball[22] it is very clear how (rare) regions of particularly weak confinement would contribute disproportionally to the effective matrix. Analytically, this effect is due to the leading quenched-disorder contribution to the replica Hamiltonian (6) before buckling is negative (as was also seen in slightly different context in[23,32]).

The methodology we present in this paper is quite general. Although we assumed the Poisson distribution for matrix confinements and take the MT as an example, it should be able to extend to other distribution functions for confinements, and other ranges of parameters can also be applied, as long as we stay in the regime of a long filament. On the other hand, short filaments cannot be analyzed with the form of the correlator G_{ab}^{-1} that Mézrad and Parisi have proposed for the trial Hamiltonian in the GVM. We showed that the dependence of the Fourier modes of the correlator changes, using the 4th-order Hamiltonian as an example. The buckling of a short filament in an elastic matrix needs to be investigated separately.

Acknowledgements

[1] D. E. Ingber, J. Cell Sci. **104**, 613 (1993).
[2] M. F. Coughlin and D. Stamenović, J. Appl. Mech. **64**, 480 (1997).
[3] A. M. R. Kabir, D. Inoue, T. Afrin, H. Mayama, K. Sada, and A. Kakugo, Sci. Rep. **5**, 17222 (2015).
[4] M. Z. Jin and C. Q. Ru, Phys. Rev. E **88**, 012701 (2013).
[5] S. Timoshenlko and J. M. Gere, Theory of elastic instability (McGraw-Hill, N. Y., 1961).
[6] O. Kratky and G. Porod, Recl. des Trav. Chim. des Pays-Bas **68**, 1106 (2010).
[7] T. Odijk, Macromolecules **28**, 7016 (1995).
[8] K. Baczynski, R. Lipowsky, and J. Kierfeld, Phys. Rev. E **76**, 061914 (2007).
[9] M. Emanuel, H. Mohrbach, M. Saya, H. Schiessel, and I. M. Kulic, Phys. Rev. E **79**, 061907 (2007).
[10] D. R. Nelson, Physica A **177**, 220 (1991).
[11] J. R. Blundell and E. M. Terentjev, Soft Matter **20**, 4015 (2009).
[12] F. Gittes, E. Meyhöfer, S. Baek, and J. Howard, Biophys. J. **70**, 418 (1996).
[13] S. L. Gupton, W. C. Salmon, and C. M. Waterman-Storer, Curr. Biol. **12**, 1891 (2002).
[14] C. P. Brangwynne, F. C. MacKintosh, S. Kumar, N. A. Geisse, J. Talbot, L. Mahadevan, K. K. Parker, D. E. Ingber, and D. A. Weitz, J. Cell Biol. **173**, 733 (2006).
[15] M. Das, A. J. Levine, and F. C. MacKintosh, Europhys. Lett. **84**, 18003 (2008).
[16] W. L. Shan, Z. Chen, C. P. Broedersz, A. A. Gumaste, W. O. Soboyejo, and C. P. Brangwynne, Soft Matter **9**, 194 (2013).
[17] B. Fabry, G. N. Maksym, J. P. Butler, M. Glogauer, D. Navajas, and J. J. Fredberg, Phys. Rev. Lett. **87**, 148102 (2001).
[18] B. R. Parry, I. V. Surovtsev, M. T. Cabeen, C. S. ÓHern, E. R. Dufresne, and C. Jacobs-Wagner1, J. Cell **156**, 182 (2014).
[19] G. T. Charras, M. Coughlin, T. J. Mitchison, and L. Mahadevan, Biophys. J. **94**, 1836 (2008).
[20] G. Salbreux, G. T. Charras, and E. Paluch, Trends Cell Biol. **22**, 536 (2012).
[21] S. F. Edwards and M. Muthukumar, J. Chem. Phys. **89**, 2435 (1988).
[22] M. Cates and R. C. Ball, J. Phys. France **49**, 2009 (1988).
[23] A. Craig, E. M. Terentjev, and S. F. Edwards, Physica A **384**, 150 (2007).
[24] P. Benetatos and E. M. Terentjev, Phys. Rev. E **82**, 13 (2010).
[25] P. Benetatos and E. M. Terentjev, Phys. Rev. E **84**, 9 (2011).
[26] V. Dotsenko, Introduction to the replica theory of disordered statistical systems (Cambridge University Press, N. Y., 2001).
[27] M. Mézard and G. Parisi, J. Phys. I **1**, 809 (1991).
[28] L. Petridis and E. M. Terentjev, J. Phys. A **39**, 9693 (2006).
[29] S. F. Edwards and P. M. Anderson, J. Phys. F. **6**, 1927 (1976).
[30] S. V. Fridrikh and E. M. Terentjev, Phys. Rev. E **60**, 1847 (1999).
[31] T. Castellani and A. Cavagna, J. Stat. Mech. Theory Exp. **2005**, P05012 (2005).
[32] P. Haronska and T. A. Vilgis., J. Chem. Phys. **101**, 3104 (1994).
[33] G. C. Wick, Phys. Rev. **80**, 268 (1950).
[34] E. Mandelkow and E.-M. Mandelkow, Curr. Opin. Struct. Biol. **4**, 171 (1994).
[35] H. Felgner, R. Frank, and M. Schliwa, J. Cell Sci. **109**, 509 (1996).
[36] F. Pampaloni, G. Lattanzi, A. Jonáš, T. Surrey, E. Frey, and E.-L. Florin, Proc. Natl. Acad. Sci. USA **103**, 10248 (2006).
[37] T. G. Kuznetsova, M. N. Starodubrseva, and N. I. Yegorenkov, Micron **38**, 824 (2007).
[38] N. Guz, M. Dokukin, V. Karaparthi, and I. Sokolov, Biophys. J. **107**, 564 (2014).
[39] K. Luby-Phelps, D. L. Taylor, and F. Lanni, J. Cell Biol. **102**, 2015 (1986).
[40] T. J. Mitchison, G. T. Charras, and L. Mahadevan, Semin. Cell Dev. Biol. **19**, 215 (2008).
[41] Y. Y. Goldschmidt, Phys. Rev. E **61**, 1729 (2000).
[42] P. Benetatos and E. M. Terentjev, Phys. Rev. E **81**, 031802 (2010).

Appendix A: Replica Hamiltonian

We discretize Eq. (4) into segments of length Δ_S, express the continuous functions of filament deflections and elastic modulus as $Y_{a,i}$ and γ_i, and then insert the probability distribution function $f[\gamma]$ of Eq. (3), to calculate the replica Hamiltonian. We particularly focus on the terms containing the local elastic modulus γ_i, as the rest of the terms will remain the same after completing the path integral over the configurations of local elastic modulus. The $f[\gamma]$ function is further approximated with the Stirling formula, $\ln n! \approx (n \ln n - n)$, when expressing it as an exponential function. The path integral then takes the form:

$$\frac{1}{\mathcal{N}} \prod_i^w \int_0^\infty d\gamma_i \exp\left[\gamma_i \nu \ln\left(\frac{\gamma_i}{\langle\gamma\rangle} \right) + \nu\left(\gamma_i - \langle\gamma\rangle\right) \right]$$
$$\times \exp\left(\frac{-\beta}{2} \gamma_i \nu \varepsilon \sum_a Y_{a,i}^2 \right) , \qquad (A1)$$

where ν is defined as the ratio (Δ_S/ε), and $\langle\gamma\rangle$ is the mean elastic modulus. Note that the exponential in the first line is the Stirling approximation for $f(\gamma_i)$, while the second is the local elastic energy term from $\sum_a H_a$ of Eq. (4). The direct implementation of these integrals is not plausible. We turn to the 'steepest decent' approximation with respect to γ_i, for the exponent of the above equation. The stationary point γ_i^* for this exponent is found out as:

$$\gamma_i^* = \langle\gamma\rangle e^{-\frac{\beta\varepsilon}{2}\sum_a Y_{a,i}^2}. \qquad (A2)$$

Taylor-expansion of the exponential function of Eq. (A1) around γ_i^* in Eq. (A2) to the second order gives a Gaussian form in the path integral:

$$\prod_i^w \left\{ \exp\left[\langle\gamma\rangle \frac{\Delta_S}{\varepsilon} \left(-1 + e^{-\frac{\beta\varepsilon}{2}\sum Y_{a,i}^2} \right) \right] \right.$$
$$\left. \times \frac{1}{\mathcal{N}} \int d\gamma_i \exp\left[-\frac{\Delta_S \left(\gamma_i - \langle\gamma\rangle\right)^2}{2\varepsilon\langle\gamma\rangle} e^{-\frac{\beta\varepsilon}{2}\sum Y_{a,i}^2} \right] \right\}. \qquad (A3)$$

The first line of Eq. (A3) now has no γ_i variable, and is part of our final result of the replica Hamiltonian. But this term has another exponential inside the exponent, and therefore is still too complicated for later GVM calculations in Section 2.3. Because of our small-deflection assumption before buckling occurs, we can Taylor-expand this exponent in terms of the summed deflections of all replicas $\sum_a Y_{a,i}^2$, and keep it to the 6th

order. The final result is further expressed as a continuous integral of dS, by assuming slowly-varying functions of deflections within each segment:

$$\prod_i^w \exp\left[\langle\gamma\rangle\frac{\Delta_S}{\varepsilon}\left(-1+e^{-\frac{\beta\varepsilon}{2}\sum Y_{a,i}^2}\right)\right]$$
$$\approx \exp\left\{\frac{-\beta\langle\gamma\rangle}{2}\int dS\left[\sum Y_a^2 - \frac{\varepsilon}{4}\left(\sum Y_a^2\right)^2 + \frac{\beta\varepsilon^2}{24}\left(\sum Y_a^2\right)^3\right]\right\}. \tag{A4}$$

We go back to the second line of Eq. (A3), which contains an apparently Gaussian path integral and the normalization factor $\mathcal{N}$. This normalization factor can be calculated using the same 'steepest descent' method. The overall result takes the form:

$$\frac{1}{\mathcal{N}}\prod_i^w\int_0^\infty d\gamma_i \exp\left[-\frac{\Delta_S\left(\gamma_i - \langle\gamma\rangle\right)^2}{2\varepsilon\langle\gamma\rangle}e^{-\frac{\beta\varepsilon}{2}\sum Y_{a,i}^2}\right]$$
$$\approx \prod_i^w \frac{\int d\gamma_i \exp\left[-\frac{\Delta_S(\gamma_i-\langle\gamma\rangle)^2}{2\varepsilon\langle\gamma\rangle}e^{-\frac{\beta\varepsilon}{2}\sum Y_{a,i}^2}\right]}{\int d\gamma_i \exp\left[-\frac{\Delta_S(\gamma_i-\langle\gamma\rangle)^2}{2\varepsilon\langle\gamma\rangle}\right]}$$
$$= \exp\left\{\sum_i \ln\frac{1 + \mathrm{erf}\left(\sqrt{e^{\varphi_i}\langle\gamma\rangle\Delta_S/2\varepsilon}\right)}{e^{\varphi_i/2}\left[1 + \mathrm{erf}\left(\sqrt{\langle\gamma\rangle\Delta_S/2\varepsilon}\right)\right]}\right\}, \tag{A5}$$

where $\varphi_i = \frac{1}{2}\beta\varepsilon\sum_a Y_{a,i}^2$ and erf means the error function. Because of the small-deflection assumption, we Taylor-expand the ln-term in terms of φ_i, and find out that each term of this series has a decaying exponential factor, $\exp\left(-\Delta_S\langle\gamma\rangle/2\varepsilon\right)$. As Δ_S increases, Eq. (A5) will eventually reduce to one and play no role in the replica Hamiltonian. This indicates that this ln-term is the error produced when we apply the 'steepest descent' approximation and express the original integral in the Gaussian form, as it is well-known that the Poisson distribution can be replaced by the Gaussian form only when the step size (the interval) is large enough.

Because this decaying exponential factor appears in the exponent of Eq. (A5), it, in fact, decays rather rapidly as Δ_S increases. There should be a suitable Δ_S value that makes this error become negligible, while the transformation into the continuum model is still applicable. In this sense, Eq. (A1) is approximately equal to Eq. (A4). We take out the thermal factor, $-\beta$, in the exponent of Eq. (A4), and together with the original terms that do not contain the local elastic modulus $\gamma(S)$, i.e. the bending energy and work done by compression, it gives the replica Hamiltonian of Eq. (6).

Appendix B: Variational free energy

In this section, we use the 4th-order case as an example, to show the origins of the pre-factor Γ_4 in Eq. (8), and then how to remove this Γ_4 factor by paring the

Fourier mode to obtain the variational free energy in Eq. (11). We start from inserting the Fourier series: $y_a = \sum_n \bar{y}_{an}\sin\left(n\pi s/l_0\right)$ into the replica Hamiltonian of Eq. (7). The integral we are dealing with is:

$$\int_0^{l_0} ds\sin\left(\frac{n_1\pi s}{l_0}\right)\sin\left(\frac{n_2\pi s}{l_0}\right)\sin\left(\frac{n_3\pi s}{l_0}\right)\sin\left(\frac{n_4\pi s}{l_0}\right)$$

The product of sin-functions can be decomposed into cos-functions, by using the identities:

$$\sin A\cdot\sin B = \frac{1}{2}\left[\cos\left(B-A\right) - \cos\left(B+A\right)\right]\ ;$$
$$\cos A\cdot\cos B = \frac{1}{2}\left[\cos\left(A+B\right) - \cos\left(A-B\right)\right].$$

Eventually eight cos-functions with a numerical factor $1/8$ in front are produced. Each of them after integration gives a Kronecker delta. For example, $\int ds\cos[(n_1 - n_2 + n_3 - n_4)\pi s/l_0] = l_0\delta(n_1 - n_2 + n_3 - n_4)$. The final result of the integrated sin-product gives $l_0\Gamma_4/8$, where Γ_4 is defined as:

$$\Gamma_4 = \delta(n_1 + n_2 + n_3 + n_4) + \delta(n_1 - n_2 + n_3 - n_4)$$
$$+ \delta(n_1 + n_2 - n_3 - n_4) + \delta(n_1 - n_2 - n_3 + n_4)$$
$$- \delta(n_1 - n_2 + n_3 + n_4) - \delta(n_1 - n_2 - n_3 - n_4)$$
$$- \delta(n_1 + n_2 + n_3 - n_4) - \delta(n_1 + n_2 - n_3 + n_4).$$

The same procedure to integrate sin-product in the 6th-order case can be applied to find out Γ_6 (with 32 deltas inside), but we will not show its result here.

We move on to calculate the variational free energy defined in Eq. (10), with the trial Hamiltonian shown in Eq. (9), and look at how to remove the deltas of Γ_4 in the 4th-order contributions of $\langle\tilde{H}_{\mathrm{rep}}\rangle_0$, that is, $\sum_{a,b}\sum_{\{n\}}-\eta l_0\Gamma_4\langle\bar{y}_{an_1}\bar{y}_{an_2}\bar{y}_{bn_3}\bar{y}_{bn_4}\rangle_0/32$.

The Gaussian form of $\langle\tilde{H}_{\mathrm{rep}}\rangle_0$ requires the Fourier modes in $\bar{y}_{an}$-product above to be paired, in order to produce a non-zero value. It follows that some of the terms in Γ_4 can never meet the pairing-requirement, if one wants to have a non-zero value from the Kronecker delta. Those with the odd number of '-' signs, e.g. $\delta(n_1 - n_2 - n_3 - n_4)$, and $\delta(n_1 + n_2 + n_3 + n_4)$ will be killed during the discussion. Only three deltas of Γ_4 remain: $\delta(1 - 2 + 3 - 4)$, $\delta(1 + 2 - 3 - 4)$, and $\delta(1 - 2 - 3 + 4)$, where the shorthand $n_1 \to 1$, and so on, is used. We will take $\sum_{\{n\}}\delta(1 - 2 - 3 + 4)\langle\bar{y}_{a1}\bar{y}_{a2}\bar{y}_{b3}\bar{y}_{b4}\rangle_0$ as an example, to show a systematic way to remove the Kronecker delta when summing over the Fourier modes n.

We consider two situations: all with the same Fourier modes, and two pairs with different modes. For cleanness, we will not explicitly write the summation for replica indices and Fourier modes for the following content of this section. In the first scenario, we need to calculate $\langle\tilde{y}_{a1}\tilde{y}_{a1}\tilde{y}_{b1}\tilde{y}_{b1}\rangle_0$, which can easily be obtained with the Wick formula:

$$\langle\tilde{y}_{a1}\tilde{y}_{a1}\tilde{y}_{b1}\tilde{y}_{b1}\rangle_0 = G_{aa}^{(1)}G_{bb}^{(1)} + 2G_{ab}^{(1)}G_{ab}^{(1)}\ , \tag{B1}$$

where the notation $\sum_{n_1}$ and $\sum_{a,b}$ are omitted, following the convention we mentioned above. Next, two pairs with different modes have two possibilities:

$$\langle \tilde{y}_{a1}\tilde{y}_{a1}\tilde{y}_{b2}\tilde{y}_{b2}\rangle_0 \tau = G_{aa}^{(1)}G_{bb}^{(2)}\tau \ ;$$
$$\langle \tilde{y}_{a1}\tilde{y}_{a2}\tilde{y}_{b1}\tilde{y}_{b2}\rangle_0 \tau = G_{ab}^{(1)}G_{ab}^{(2)}\tau \ , \qquad \text{(B2)}$$

where the factor τ is to ensure these two modes are different, $\tau = 1 - \delta(1-2)$. Combining Eqs. (B1) and (B2) gives the result for this example. The rest of the deltas inside Γ_4 and the Γ_6 term of Eq. (8) can be dealt with in the same procedures, to find out $\tilde{H}_{\text{rep}}$ and then obtain the variational free energy $\tilde{F}$. Here, we only show the final result:

$$\tilde{F} = -\frac{1}{2}\sum_n \text{Tr}\ln\underline{\underline{G}}(n) + \frac{l_0\psi(1)}{2}G_{aa}^{(1)}$$

$$-\frac{\eta l_0}{32}\left(4G_{ab}^{(1)}G_{ab}^{(2)} + 2G_{aa}^{(1)}G_{bb}^{(2)} + 2G_{ab}^{(1)}G_{ab}^{(1)} + G_{aa}^{(1)}G_{bb}^{(1)}\right)$$

$$+\frac{wl_0}{192}\left(32G_{ab}^{(1)}G_{ac}^{(2)}G_{bc}^{(3)} + 24G_{aa}^{(1)}G_{bc}^{(2)}G_{bc}^{(3)} + 4G_{aa}^{(1)}G_{bb}^{(2)}G_{cc}^{(3)}\right.$$

$$+48G_{ab}^{(1)}G_{ac}^{(1)}G_{bc}^{(2)} + 24G_{aa}^{(1)}G_{bc}^{(1)}G_{bc}^{(2)} + 6G_{aa}^{(1)}G_{bb}^{(1)}G_{cc}^{(2)}$$

$$+12G_{ac}^{(1)}G_{ac}^{(1)}G_{bb}^{(2)} - 3G_{ab}^{(1)}G_{bb}^{(2)}G_{cc}^{(1+2)} - 6G_{ab}^{(1)}G_{ab}^{(2)}G_{cc}^{(1+2)}$$

$$\left.-12G_{ab}^{(1)}G_{cc}^{(2)}G_{ab}^{(1+2)} - 24G_{ac}^{(1)}G_{bc}^{(2)}\ G_{ab}^{(1+2)}\right) \ , \qquad \text{(B3)}$$

where the definition of $\psi(1)$ is given below Eq. (11), and the summation over replica indices and Fourier modes that show up in individual terms are omitted. For instance, the term $G_{ab}(1)G_{ab}(2)$ is summed over a, b, n_1 and n_2 and $G_{aa}(1)G_{bb}(1)$ is summed over a, b, and n_1 (note that not over n_2). The superscript $1 + 2$ means $n_1 + n_2$, and it is a result from the 6th-order case that gives the requirement $n_1 = n_3$, $n_2 = n_4$ and $n_5 = n_6 = n_1 + n_2$, when discussing the pairing to remove $\delta(n_1 + n_2 + n_3 + n_4 - n_5 - n_6)$, and other similar deltas.

For a long filament, the full expression of $\tilde{F}$ of Eq. (B3) can be approximated by finding out l_0-scaling in each individual term, so as to recognize which of them are the major contributions, when taking the limit $l_0 \to \infty$. The summation over Fourier modes $\sum_n$ is replaced with the integral $\int dn$, and we further use the wavenumber $q = n\pi/l_0$ as the new variable for integration, therein, $\int dn \to l_0 \int dq/\pi$. And we notice that $G_{ab}(n)$, which can be readily obtained from its symmetrical inverse of Eq. (9), contains the $1/l_0$ factor inside:

$$G_{ab}(n) = \frac{1}{l_0\Lambda}\left[\delta_{ab} - \frac{\sigma}{\Lambda + m\sigma}\right]. \qquad \text{(B4)}$$

With q-transformation of $\sum_n$ and G_{ab} expression above, we are now ready to do the scaling analysis and find that, for example:

$$G_{ab}^{(1)}G_{ab}^{(2)} \propto l_0^2 * \frac{1}{l_0^2} = 1 \ ; \ G_{aa}^{(1)}G_{bb}^{(1)} \propto l_0 * \frac{1}{l_0^2} = \frac{1}{l_0} \ ,$$

where the first l_0 factor on the right hand side is from the q-transformation (l_0^2 from the double sum, $\sum_{n_1,n_2}$, and l_0 from one sum, $\sum_{n_1}$), while the second factor is from the product of two $G_{ab}(n)$. As $l_0 \to \infty$, one can find out which terms are more prevailing. The similar analysis can be applied to the rest of terms of Eq. (B3). It turns out that the terms, with the number of sums over Fourier modes equal to the number of G_{ab} inside the product, has l_0 factor, e.g. $wl_0 G_{ab}^{(1)}G_{ac}^{(2)}G_{bc}^{(1)}/6$ (the first term in the third line of Eq. (B3)), while other terms will have no l_0 factor, except for the term $-\sum_n \text{Tr}\ln\underline{\underline{G}}(n)/2$ which we will have to discuss separately.

If the matrix has the form: $M_{ab} = A\delta_{ab} - ABI_{ab}$, where δ_{ab} and I_{ab} are elements of the identity matrix and the matrix of ones, respectively, and A and B are constants or functions independent of the matrix indices a and b. $\ln\underline{\underline{M}}$ can be expressed as:

$$\left(\ln\underline{\underline{M}}\right)_{ab} = (\ln A)\delta_{ab} + \frac{1}{d}\ln(1 - dB)I_{ab} \ , \qquad \text{(B5)}$$

where d is the dimension of the matrix. The trace of $\ln\underline{\underline{M}}$ above is simply:

$$\text{Tr}\ln\underline{\underline{M}} = d\ln A + \ln(1 - dB) \ . \qquad \text{(B6)}$$

In fact, our correlator $\underline{G}$ of Eq. (14) has the same structure as $\underline{M}$ above, and we can use Eq. (B6) to calculate $\text{Tr}\ln\underline{G}$. Recall that our purpose here is simply find the l_0 scaling in $\sum_n \text{Tr}\ln\underline{\underline{G}}(n)$. We recognize that the A factor in Eq. (B5) has the scaling $1/l_0$ in the case of our correlator $\underline{G}$ from Eq. (B4), while B does not contain any l_0 factor. $\sum_n \text{Tr}\ln\underline{\underline{G}}(n)$ takes the form $\sum_n(-d\ln l_0 + C)$, where C is a function irrelevant to l_0. Following the q-transformation for the n-sum, $\sum_n \text{Tr}\ln\underline{\underline{G}}(n) \propto (d\, l_0 \ln l_0 - Cl_0)$, and it is therefore one of the major contributions in Eq. (B3). Overall, the major contributions of the variation free energy in the long filament case is presented in Eq. (11) in the main content. As for the short-filament case, one has to use the full expression of the variational free energy, Eq. (B3).

Appendix C: Optimization equation

In this section, we start from the approximate variational free energy in the long filament case, Eq. (11), find out its optimization equation with respect to G_{ij}, and show the n-dependence inside Λ of Eq. (9). Then we discuss the short-filament case to show that this n-dependence will be changed, from its optimization equation. We will not present the full calculation detail to obtain the optimization equation in the short-filament case, but instead equip the readers with the necessary tools used through this procedure.

The optimization equation is obtained from the condition $\delta\tilde{F}/\delta G_{ij}(n) = 0$ (using Eq. (11) for the long-filament case), and further simplified by taking the limit: the total number of replicas goes to zero, $m \to 0$. We introduce a useful identity for the calculation of this derivative $\delta\tilde{F}/\delta G_{ij}(n)$, particularly for terms of $\tilde{H}_{\mathrm{rep}}$ inside $\tilde{F}$:

$$\frac{\delta G_{ab}(n_1)}{\delta G_{ij}(n)} = \delta_{ia}\delta_{jb}\delta_{n_1 n} , \qquad (C1)$$

where these deltas are Kronecker deltas, and note that the summation convention for repeated indices is not used here. We calculate the terms of the second line in Eq. (11) as an example:

$$\sum_{a,b}\sum_{n_1,n_2}\frac{\delta G_{ab}(n_1)\delta G_{ab}(n_1)}{\delta G_{ij}(n)} = 2\sum_{n_1}G_{ij}(n_1) ;$$

$$\sum_{a,b}\sum_{n_1,n_2}\frac{\delta G_{aa}(n_1)\delta G_{bb}(n_2)}{\delta G_{ij}(n)} = 2\delta_{ij}\sum_{a}\sum_{n_1}G_{aa}(n_1)$$

$$= 2\delta_{ij}m\sum_{n_1}G_{11}(n_1) ,$$

where in the last line, the replica symmetry of G_{ab} can extract an m factor out, and this term will vanish as taking the limit $m \to 0$. One can repeat the same procedure, keep the terms that survive after taking $m \to 0$, and eventually will reach the result:

$$G_{ab}^{-1}(n) \approx l_0\ \psi(n)\ \delta_{ab}$$

$$+\frac{l_0}{2}\left(w\sum_{i}^{m}\sum_{\{n\}}G_{ai}^{(1)}G_{ib}^{(2)} - \eta\sum_{n_1}G_{ab}^{(1)}\right)I_{ab} , \quad (C2)$$

where $\psi(n)$ is defined below Eq. (11). We further remove the embedded m-dependence of Eq. (13), by inserting the replica symmetrical form of G_{ab} in Eq. (B4):

$$\sum_{i}^{m}\sum_{\{n\}}G_{ai}^{(1)}G_{ib}^{(2)} = \sum_{\{n\}}[A(1)A(2)\delta_{ab} - 2A(1)B(2)I_{ab}$$

$$+ mB(1)B(2)I_{ab}] , \qquad (C3)$$

where the shorthand $A(n)$ and $B(n)$ are the matrix elements defined by $G_{ab}(n) = A\delta_{ab} - BI_{ab}$, with the detailed $G_{ab}(n)$ expression given in Eq. (B4). The m factor of Eq. (C3) is from the sum: $\sum_{i}^{m}I_{ai}I_{ib}$, and hence the last term will vanish at $m = 0$.

We now express the optimization equation (C2) in terms of Λ and σ, by inserting G_{ab}^{-1} of Eq. (9), G_{ab} of Eq. (B4) and removing m-dependence as shown in Eq. (C3). The diagonal element generates the optimization equation of the form:

$$\Lambda(n) \approx \psi(n) - \frac{\eta}{2l_0}\sum_{n}\frac{1}{\Lambda(n)} + \frac{w}{2l_0^2}\left(\sum_{n}\frac{1}{\Lambda(n)}\right)^2 . \quad (C4)$$

We observe that the n-dependence of $\Lambda(n)$ is given by $\psi(n)$, while the last two terms on the right hand side of

Eq. (C4) are simply a constant independent of n. We can define this constant as λ, giving $\Lambda = \psi + \lambda$, which can be put back into Eq. (9) and recover $G_{ab}^{-1}(n)$ of Eq. (12) used for a long filament (beware that ψ has the same expression as ϑ).

We now consider the short-filament case that requires the full expression of the variational free energy of Eq. (B3). We follow similar calculation procedures of the long-filament case, by using Eqs. (C1) and (B4), and following the same analysis of m-dependence. The final optimization equation for the diagonal part in the short-filament case has the form:

$$\left\{\frac{l_0}{2}\ \psi(n) - \frac{l_0}{2}\Lambda(n) - \frac{\eta}{4\Lambda(n)} + \frac{w}{2l_0\Lambda(n)}\sum_{n_1}\frac{1}{\Lambda(n_1)}\right.$$

$$\left.- \frac{w}{4l_0}\sum_{n_1}\frac{1}{\Lambda(n_1)\Lambda(n_1+n)} + \frac{u_n w}{8l_0}\sum_{n_1=1}^{n-1}\frac{1}{\Lambda(n_1)\Lambda(n-n_1)}\right\}$$

$$+ \left\{\frac{-\eta}{4}\sum_{n_1}\frac{1}{\Lambda(n_1)} + \frac{w}{4l_0}\left(\sum_{n_1}\frac{1}{\Lambda(n_1)}\right)^2\right.$$

$$\left.+ \frac{w}{4l_0}\sum_{n_1}\frac{1}{\Lambda^2(n_1)}\right\} = 0 , \qquad (C5)$$

where u_n is a step function that equals to one when $n \geq 2$, otherwise zero, and is a result when calculating $\sum_{n_1,n_2}\delta G_{ab}(n_1+n_2)/\delta G_{ij}(n)$. There, we use the change of variable $n_3 \equiv n_1 + n_2$, and the sum $\sum_{n_1,n_2=1}^{\infty}$ is transformed to $\sum_{n_3=2}^{\infty}\sum_{n_1=1}^{n_3-1}$ (note the change of the upper and lower limits of the sums).

Equation (C5) can recover the result of Eq. (C4), following the same analysis of l_0 scaling shown in Appendix B to obtain the approximate variational free energy. The first bracket of Eq. (C5) contains functions of n and is used to investigate the n-dependence in Λ, while the second bracket is simply an n-independent terms and can be denoted as a constant $2l_0\lambda$, without losing any generality.

Nevertheless, the n-dependence of Λ is hard to obtain in Eq. (C5) for the 6th-order case (with the w coefficient). We consider a simpler 4th-order case, letting $w = 0$ in Eq. (C5), and write it in the form:

$$\frac{l_0}{2}\psi(n) - \frac{l_0}{2}\Lambda(n) - \frac{\eta}{4\Lambda(n)} + 2l_0\lambda = 0 , \qquad (C6)$$

where $2l_0\lambda$ is defined as a constant given by the second bracket of Eq. (C5) with $w = 0$ there. This equation is quadratic and we can obtain the n-dependence of Λ as:

$$\Lambda(n) = \frac{1}{2}\left[\psi(n) + \lambda + \sqrt{(\psi(n)+\lambda)^2 - \eta/2l_0}\right]. \quad (C7)$$

Note that if letting $l_0 \to \infty$, the above Λ expression reduces to Eq. (12) for a long filament. It can also be seen that the $\Lambda(n)$ in the 4th-order case for the short filament has totally a different form and n-dependence. Therefore,

for the short-filament case, our assumed n-dependence of G_{ab}^{-1} in the main context is not applicable, and can only be used for the long filament. The following analysis and results of buckling we obtain there cannot extend to the short filaments.

Appendix D: Self-check of the mesh size at critical points

In the continuum model, a careful check should be made by comparing the non-dimensional mesh size, i.e. the spacing between confinements, with the most dominant buckling wavelength. Only when the mesh size is smaller than this buckling wavelength, the use of the continuum model is valid, as will not violate the assumption of smooth and slowly-varying deflections within the segment Δ_S.

The non-dimensional mesh size l_m is given as: $l_m = \Delta/\text{æ}$, where we remind that æ and Δ are non-dimensional mean elastic modulus and elastic strength of single confinement, respectively. To find out the non-dimensional wavelength λ_d of the most dominant buckling mode, we need to obtain the mean-squared Fourier amplitude of mode n_1: $\langle \bar{y}_{n_1} \bar{y}_{n_1} \rangle$. From the quench-averaging definition given in Eq. (5) and the trial Hamiltonian of Eq. (9) with the correlator G_{ab}^{-1} given in Eq. (12), $\langle \bar{y}_n \bar{y}_n \rangle$ is calculated through:

$$
\begin{aligned}
\langle \bar{y}_{n_1} \bar{y}_{n_1} \rangle &= \lim_{m \to 0} \int \left(\prod_{a=1}^{m} \prod_{n} d\bar{y}_{an} \right) \bar{y}_{1n} \bar{y}_{1n} e^{-\tilde{H}_0} \\
&= \lim_{m \to 0} \left\{ G_{11}(n_1) \exp \left[\frac{1}{2} \mathrm{Tr} \ln \left(2\pi \underline{\underline{G}} \right) \right] \right\} \\
&= \frac{1}{l_0 \left(\vartheta(n_1) + \lambda_0 \right)} = \frac{2}{l_0 \left(kq^4 - pq^2 + \alpha \right)} \quad , \quad \text{(D1)}
\end{aligned}
$$

where $\mathrm{Tr} \ln (2\pi \underline{\underline{G}})$ reduces to one, as can be checked with help of Eq. (B6) (letting $d = m = 0$ and notice that A and B are simply a constant at $m = 0$ in our G_{ab} case). The definition of ϑ can be found in Eq. (12) and λ_0 is the solution of the optimization equation with the limit $m \to 0$, see Eq. (13). In the final expression, we use the wavenumber q (defined as $n\pi/l_0$) and α to replace n and λ.

From Eq. (D1), the most dominant wavenumber q_d, together with the corresponding buckling wavelength λ_d, can be obtained as:

$$
q_d = \sqrt{\frac{p}{2k}} \quad ; \quad \lambda_d = \frac{2\pi}{q_d} = 2\pi \sqrt{\frac{2k}{p}} \quad . \quad \text{(D2)}
$$

The self-check of the validity of the continuum model is to compare λ_d above with the non-dimensional mesh size $l_m = \Delta/\text{æ}$.

We are particularly interested in investigating whether the validity of the continuum model still holds at the occurrence of the critical phenomenon. We can obtain the buckling force $\langle p_c \rangle$ at this critical point, by inserting

Δ_c of Eq. (21) into the p_{2c} expression of Eq. (22), and we subsequently put the obtained result into Eq. (D2) to find the dominant wavelength λ_d^c. It is :

$$
\lambda_d^c = 4\sqrt{2}\pi \sqrt{\frac{k}{8\sqrt{\text{æ}k} - k^{1/3} \left(2\text{æ} \, l_m^c \right)^{2/3}}} \quad , \quad \text{(D3)}
$$

where l_m^c is 'upper boundary' of the non-dimensional mesh size at the critical phenomenon and is given as $l_m^c = 0.5 * (k/\text{æ})^{1/4}$. The inequality to be proven is:

$$
\begin{aligned}
\lambda_d^c &= 4\sqrt{2}\pi \sqrt{\frac{k}{8\sqrt{\text{æ}k} - k^{1/3} \left(2\text{æ} \, l_m^c \right)^{2/3}}} > l_m^c \\
&\to \frac{k}{8\sqrt{\text{æ}k} - k^{1/3} \left(2\text{æ} \, l_m^c \right)^{2/3}} > \frac{(l_m^c)^2}{32\pi^2} \\
&\to \frac{1}{7} \sqrt{\frac{k}{\text{æ}}} > \frac{1}{128\pi^2} \sqrt{\frac{k}{\text{æ}}} \quad , \quad \text{(D4)}
\end{aligned}
$$

where the last line we expand l_m^c in k and æ. This inequality always holds, so the validity of our continuum model can extend to the critical point we observe in Section 3.2.

Appendix E: Force-displacement profile

The displacement ΔL under the small-deflection assumption we use for the filament Hamiltonian takes the form:

$$
\Delta L = \frac{1}{2} \int dS \left(\frac{dY}{dS} \right)^2 .
$$

The above relation can be re-written in the non-dimensional form, following the same procedure in the end of Section 2.1, and then using the Fourier series $y = \sum_n \bar{y}_n \sin(n\pi/l_0)$, which gives:

$$
\Delta L = \frac{\zeta}{2} \int ds \left(\frac{dy}{ds} \right)^2 = \frac{\zeta l_0}{4} \sum_n \bar{y}_n^2 \left(\frac{n\pi}{l_0} \right)^2 \quad , \quad \text{(E1)}
$$

where ζ is the length scale we choose for non-dimensionalization, with all other non-dimensional variables or parameters defined below Eq. (7).

The quench-averaged displacement $\langle \Delta L \rangle$ is easily obtained by combining the above equation with the relation of $\langle \bar{y}_n \bar{y}_n \rangle$ given in Eq. (D1). For a long-filament, the n-sum can be replaced with the n-integral, and then rewritten in the q-form (with $q = n\pi/l_0$). We obtain the relation:

$$
\left\langle \frac{\Delta L}{L_0} \right\rangle = \frac{1}{2\pi} \int_0^\infty \frac{q^2}{kq^4 - pq^2 + \alpha} dq . \quad \text{(E2)}
$$

Note that L_0 is the filament length with the relation $L_0 = l_0 \zeta$, and the integral limits of q are zero and ∞, due to our

assumption of a continuous long filament. Equation (E2) after integration gives:

$$\left\langle \frac{\Delta L}{L_0} \right\rangle = \left. \frac{-A_1 \tan^{-1}\left(\frac{\sqrt{2k}}{A_1}q\right) + A_2 \tan^{-1}\left(\frac{\sqrt{2k}}{A_2}q\right)}{\pi\sqrt{8k(p^2 - 4k\alpha)}} \right|_{q=0}^{\infty}$$

$$= \frac{-A_1 + A_2}{4\sqrt{2k(p^2 - 4k\alpha)}} \tag{E3}$$

with

$$A_1 = \sqrt{-p - \sqrt{p^2 - 4k\alpha}} \text{ and } A_2 = \sqrt{-p + \sqrt{p^2 - 4k\alpha}} \;.$$

To simplify $-A_1 + A_2$ in the numerator, we need to know whether $p^2 - 4k\alpha$ is positive or negative, so that we can find the expressions of A_1 and A_2 in the complex plane. By looking back at Eq. (19) of $p_\pm$, we can see that both of these p functions sit below the asymptote $p = 2\sqrt{k\alpha}$, and therefore $p^2 - 4k\alpha$ is always negative. This is a result coming from the restriction that the correlator $\underline{\underline{G}}^{-1}$ of our trial Gaussian Hamiltonian in Eq. (12) must be positive for all n values, or the Gaussian integral becomes divergent and ill-defined. With the condition $p^2 - 4k\alpha < 0$, we find that $-A_1 + A_2$ is purely a imaginary number:

$$-A_1 + A_2 = \sqrt{2}\sqrt{p + 2\sqrt{k\alpha}} \; i \;. \tag{E4}$$

Inserting the above relation back into Eq. (E3) and be careful that $\sqrt{p^2 - 4k\alpha}$ is also purely imaginary, the i factor therefore cancels off, and we will arrive at the displacement expression used in Eq. (24).